AN IMMERSED CROUZEIX-RAVIART FINITE ELEMENT METHOD FOR NAVIER-STOKES EQUATIONS WITH MOVING INTERFACES

JIN WANG, XU ZHANG, AND QIAO ZHUANG*

Abstract. In this article, we develop a Cartesian-mesh finite element method for solving Navier-Stokes interface problems with moving interfaces. The spatial discretization uses the immersed Crouzeix-Raviart nonconforming finite element introduced in [29]. A backward Euler full-discrete scheme is developed which embeds Newton's iteration to treat the nonlinear convective term. The proposed IFE method does not require any stabilization terms while maintaining its convergence in optimal order. Numerical experiments with various interface shapes and jump coefficients are provided to demonstrate the accuracy of the proposed method. The numerical results are compared to the analytical solution as well as the standard finite element method with body-fitting meshes. Numerical results indicate the optimal order of convergence of the IFE method.

Key words. Navier-Stokes, interface problems, nonconforming immersed finite element methods, moving interface.

1. Introduction

Multi-phase immiscible incompressible flows with embedded interfaces are widely present in many physical phenomena. The related simulations appear in many branches of science and engineering, such as fluid dynamics, biology, medical sciences, and geology [9, 12, 13, 41, 49], to name just a few. The dynamics of the two-phase (or multi-phase) flows are governed by the well-known Navier-Stokes (NS) equations, or Stokes equations for creeping flows, along with the enforcement of jump conditions at interfaces. Physical parameters of the flows, such as density and viscosity coefficients, are usually discontinuous across the fluid interface [1, 9, 17, 29, 49].

In this article, we consider a two-dimensional interface problem that arises in a two-phase flow governed by the NS equation. Let $\Omega \subset \mathbb{R}^2$ be an open bounded domain separated by an interface $\Gamma(t)$ into two disjoint subdomains $\Omega^-(t)$ and $\Omega^+(t)$. Consider the following unsteady NS equation (NSE) in the velocity-stress-pressure form:

(1a)
$$\boldsymbol{u}_t - \nabla \cdot \sigma(\boldsymbol{u}, p) + (\boldsymbol{u} \cdot \nabla)\boldsymbol{u} = \boldsymbol{f} \text{ in } \Omega^-(t) \cup \Omega^+(t) \times [0, T],$$

(1b)
$$\nabla \cdot \boldsymbol{u} = 0 \quad \text{in } \Omega \times [0, T],$$

(1c)
$$\mathbf{u} = 0 \quad \text{on } \partial\Omega \times [0, T],$$

(1d)
$$u(x,0) = u_0, p(x,0) = p_0 \text{ in } \Omega,$$

where u represents the velocity field and p represents the pressure. The stress tensor $\sigma(u, p)$ is defined by

$$\sigma(\boldsymbol{u}, p) = 2\mu \boldsymbol{\epsilon}(\mathbf{u}) - p\boldsymbol{I},$$

Received by the editors January 16, 2022 and, in revised form, May 25, 2022. 2000 Mathematics Subject Classification. 35R05, 65N30.

 $^{{}^*\}mathrm{Corresponding}$ author.

where $\epsilon(\boldsymbol{u}) = (\nabla \boldsymbol{u} + (\nabla \boldsymbol{u})^t)/2$ is the strain tensor and \boldsymbol{I} is the identity tensor. The viscosity coefficient $\mu(\boldsymbol{x})$ is discontinuous across the interface $\Gamma(t)$, which is a positive piecewise-constant function defined by

(2)
$$\mu(\boldsymbol{x}) = \begin{cases} \mu^{-} & \text{if } \boldsymbol{x} \in \Omega^{-}(t), \\ \mu^{+} & \text{if } \boldsymbol{x} \in \Omega^{+}(t). \end{cases}$$

Across the interface, the following homogeneous velocity and stress jump conditions are enforced

(3a)
$$[\boldsymbol{u}]_{\Gamma} = \mathbf{0} \text{ on } \Gamma(t),$$

(3b)
$$[\sigma(\boldsymbol{u}, p)\mathbf{n}]_{\Gamma} = \mathbf{0} \text{ on } \Gamma(t),$$

where the jump $[\cdot]_{\Gamma}$ is defined by $[\mathbf{v}]_{\Gamma} := \mathbf{v}^+|_{\Gamma} - \mathbf{v}^-|_{\Gamma}$, and \mathbf{n} is the unit normal vector to the interface Γ pointing from Ω^- to Ω^+ . We also note that when $\mu(\boldsymbol{x})$ is a piecewise constant, due to the divergence condition (1b), the momentum equation (1a) can be written as

(4)
$$\mathbf{u}_t - \mu \Delta \mathbf{u} + (\mathbf{u} \cdot \nabla) \mathbf{u} + \nabla p = \mathbf{f} \quad \text{in } (\Omega^-(t) \cup \Omega^+(t)) \times [0, T].$$

Under this framework, the stress jump condition (3b) can be modified as follows

(5)
$$[(\mu \nabla \boldsymbol{u} - p\boldsymbol{I}) \, \boldsymbol{n}]_{\Gamma} = \boldsymbol{0}.$$

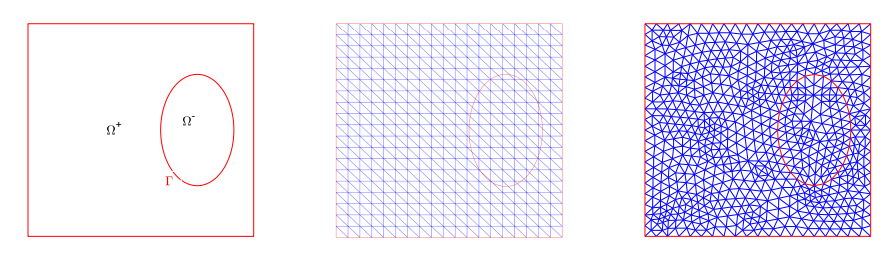


FIGURE 1. a domain with an interface (left), a non-body-fitting mesh (middle) and a body-fitting mesh (right).

The Navier-Stokes equations sans an interface are widely studied in the context of finite element methods, including classical finite element methods [16, 18], discontinuous Galerkin (DG) finite element methods [10, 15, 45, 47], and weak Galerkin finite element methods [27, 46, 51]. Those finite element methods can be extended to solve pertinent interface problems provided that body-fitting meshes are employed. However, such body-fitting restriction may hinder the efficiency in solving interface problems with evolving interfacial geometries and locations because the mesh has to be generated repeatedly according to each interface configuration. Many numerical methods based on interface-independent meshes have been developed, such as cut finite element method (CutFEM) [5, 6, 7, 42], immersed interface method (IIM) [33], extended finite element method (XFEM)[14], partition of unity finite element method (PUFEM) [44] and matched interface and boundary (MIB) [53] method. These unfitted-mesh numerical methods employ modified weak formulations or revised finite element functions around the interface to capture the interfacial jump behaviors. We refer the readers to [11, 17, 26, 43] for CutFEM, [34] for IIM, [48] for XFEM, [4] for PUFEM, and [52] for MIB applied to NS moving interface problems. An illustration of a body-fitting mesh and a non-body-fitting mesh is given in Figure 1.

Immersed finite element (IFE) methods are also a class of methods that can solve the interface problems on interface-independent meshes. Unlike unfitted numerical methods (such as CutFEMs and IIM) that employ suitable formulation around the interface, IFE methods locally construct special approximation functions on the elements cut by the interface to capture the jump behavior at the interface. In [32], the linear IFE space and its approximation capability were discussed for 2D elliptic interface problems. After that, many investigations regarding IFE methods for elliptic interface problems are conducted, including partially-penalized IFE (PPIFE) methods [36], elliptic operator with nonhomogeneous jump [24], nonconforming IFE methods [37], higher degree IFE methods [2, 19, 54]. IFE methods have also been extended to time-dependent interface problems governed by parabolic equations [20, 38, 40, 50] and hyperbolic equations [3]. IFE methods are also developed to solve interface problems governed by systems of equations, such as linear elasticity [22, 23, 39].

In recent years, IFE methods have been extended to solve Stokes interface problems. For instance, the immersed DG method based on Q_1 - Q_0 element (Q_1 : piecewise bilinear polynomial space; Q_0 : piecewise constant space on quadrilateral meshes) was developed in [1]. A class of nonconforming IFE methods based on Crouzeix-Raviart (CR)- P_0 element (P_0 : piecewise polynomial space on triangular meshes) and Rannacher-Turek rotated Q_1 - Q_0 element were recently introduced in [29]. A mixed conforming-nonconforming P_1 IFE space was introduced in [30, 31]. In addition, a Taylor-Hood P_2 - P_1 immersed finite element and the corresponding PPIFE method were developed in [8].

To simulate more general fluid flow interface problems instead of just creeping flow governed by Stokes equations, the nonlinear Navier-Stokes equations must be considered as they appear in almost all real simulations. The nonlinear convective acceleration and the evolving fluid interface make the NSE moving interface problems more challenging to solve than the Stokes interface problems [1, 8, 29, 30, 31]. To the best of our knowledge, there is no literature on the numerical study of NSE moving problems using IFE methods. We note that for the NS interface problems, the velocity and stress jump conditions in (3a) and (3b) are the same as in the Stokes interface problems [28]; therefore, there is no need to construct new IFE spaces for NS interface problems. We can employ the existing IFE spaces for Stokes interface problems [1, 29, 30, 8] directly to study NS interface problems. To handle the nonlinear convection, we adopt the Newton's method in our full-discrete scheme. In addition, we use the backward Euler scheme for time marching due to its A-stability and simplicity. Among those existing IFE spaces [1, 29, 30, 8], we note that the CR- P_0 IFE spaces introduced in [29] have two prominent features: (i) they impose weak continuity such that the average integral value across the edges is continuous; thus there is no need to include stabilized terms. As a result, the numerical scheme is much simpler comparing to the PPIFE method [8] and the DG scheme [1]. (ii) On the same Cartesian mesh, there are often less degrees of freedom for CR-P₀ than in the immersed DG space [1] and Taylor-Hood IFE space [8]; thus, it is computationally more efficient. These two features motivate us to use the CR-P₀ IFE spaces to investigate the NSE with moving interfaces presented in (1)-(3) due to its simplicity and efficiency.

The layout of the rest of the article is as follows: Section 2 introduces the notations and assumptions to be used in this article. Section 3 is devoted to introduce the semi-discrete and full-discrete nonconforming IFE methods with Newton's method for the NS interface problem (1)-(3). Numerical examples with different

interface configurations and viscosity coefficients are given in Section 4 to demonstrate the accuracy of the proposed IFE method in solving NS interface problems. Finally, a brief conclusion is drawn in Section 5.

2. Notations and Preliminaries

In this section, we introduce the notations and assumptions to be used in this article, followed by a brief recall of the $CR-P_0$ IFE space in [29].

To this point, we assume that $\Omega \subset \mathbb{R}^2$ is a polygonal domain. Let \mathcal{T}_h be a triangular mesh of Ω whose set of nodes and set of edges are denoted by \mathcal{N}_h and \mathcal{E}_h , respectively. Note that the mesh \mathcal{T}_h is independent of the location of the interface $\Gamma(t)$ at any time t. We make the following assumptions on the mesh:

- **(H1)** At any time t, the interface $\Gamma(t)$ can only intersect an element with not more than two points.
- **(H2)** At any time t, the interface $\Gamma(t)$ is a piecewise C^2 function such that for every element $T \in \mathcal{T}_h$, if $\Gamma(t) \cap T \neq \emptyset$, then $\Gamma(t) \cap T$ is a C^2 function in T.

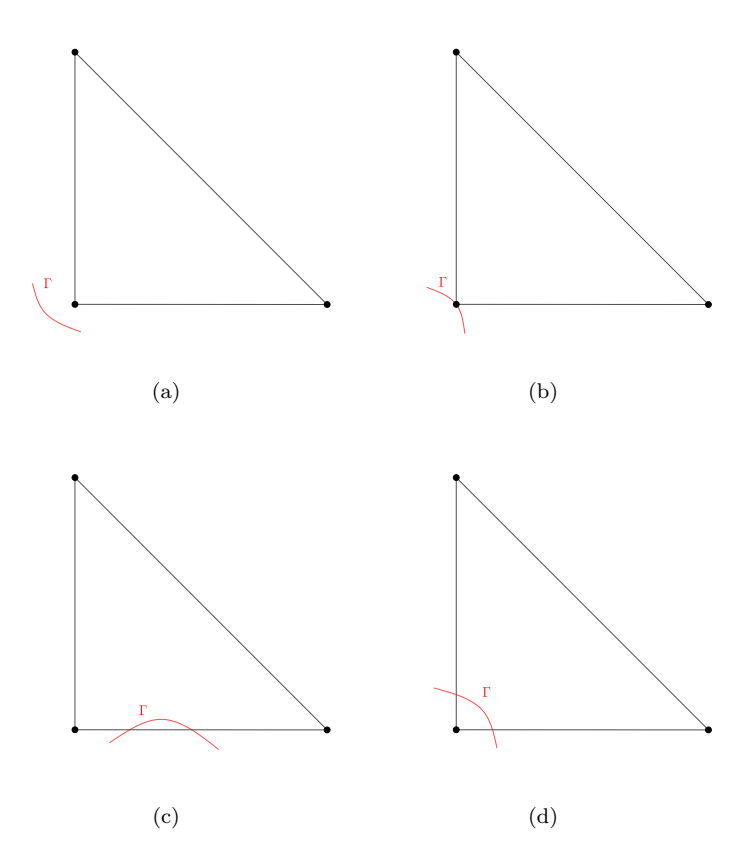


FIGURE 2. an interface intersects an element at (a) no point; (b) one point; (c) two points on the same edge; (d) two points on different edges.

If the interface $\Gamma(t)$ intersects an element T with zero or one point, then T is considered as a non-interface element. In addition, if the interface $\Gamma(t)$ intersects an element T at two distinct points but on the same edge, then T is also considered

as a non-interface element. If the interface $\Gamma(t)$ intersects an element T at two distinct points on two different edges, then T is considered as an interface element. See Figure 2 for an illustration. We note that the reason we can treat the element where the interface intersects the element at two different points on the same edge (Figure 2 (c)) as a non-interface element is: Utilizing Lemma 3.2 of [21], we can show that the area of the region bounded by the interface and the edge is $\mathcal{O}(h_T^3)$ (h_T is the diameter of the element), thus this region can be ignored compared to the element. We use $\mathcal{T}_h^i(t)$ and $\mathcal{T}_h^n(t)$ to denote the set of interface elements and non-interface elements at time t, respectively. Here, the background mesh \mathcal{T}_h is time independent, but the distribution of $\mathcal{T}_h^i(t)$ and $\mathcal{T}_h^n(t)$ changes with time. They satisfy $\mathcal{T}_h = \overline{\mathcal{T}_h^i(t)} \cup \overline{\mathcal{T}_h^n(t)}$ at any time t. Similarly, we let $\mathcal{E}_h^i(t)$ and $\mathcal{E}_h^n(t)$ be the set of interface edges and the set of non-interface edges at time t, respectively. In addition, we use $\mathring{\mathcal{E}}_h$ and \mathcal{E}_h^b for the set of interior edges and boundary edges, respectively.

For each element $T \in \mathcal{T}_h$, we define its index set as $\mathcal{I}_T = \{1, 2, 3\}$. Let A_i , $i \in \mathcal{I}_T$ be the vertices of T which are listed counterclockwise (from A_1 to A_3), and denote the edges of T to be $e_i = \overline{A_i A_{i+1}}$ for i = 1, 2, $e_3 = \overline{A_3 A_1}$. On a non-interface element $T \in \mathcal{T}_h^n$, the standard CR- P_0 finite element functions are employed to approximate the velocity and the pressure. To be more specific, let $\psi_{j,T} \in \mathbb{P}_1$, $j \in \mathcal{I}_T$ be the standard linear Lagrange shape functions on $T \in \mathcal{T}_h^n$ such that

(6)
$$\frac{1}{|e_i|} \int_{e_i} \psi_{j,T}(x,y) ds = \delta_{ij}, \ \forall i, j \in \mathcal{I}_T,$$

which is used to approximate the component of the velocity. Meanwhile, the pressure is approximated by the piecewise constant function space \mathbb{P}_0 . For the 2D Navier-Stokes problem, the components of the velocity and the pressure constitute a vector-valued finite element space, denoted by $S_h^{non}(T) = \mathbb{P}_1(T) \times \mathbb{P}_1(T) \times \mathbb{P}_0(T)$. For j = 1, 2, ..., 7, let

$$\psi_{j,T} = \begin{bmatrix} \psi_{j,T} \\ 0 \\ 0 \end{bmatrix} \text{ for } j \in \mathcal{I}_T, \ \psi_{j,T} = \begin{bmatrix} 0 \\ \psi_{j-3,T} \\ 0 \end{bmatrix} \text{ for } j-3 \in \mathcal{I}_T, \ \psi_{j,T} = \begin{bmatrix} 0 \\ 0 \\ 1 \end{bmatrix} \text{ for } j=7.$$

Then the local $CR-P_0$ finite element space on the non-interface element can be written as

(8)
$$\mathbf{S}_h^{non}(T) = \operatorname{Span}\{\boldsymbol{\psi}_{i,T}, j = 1, 2, \cdots, 7\}, \ \forall T \in \mathcal{T}_h^n.$$

On the interface elements, we note that the NS interface problems in (1) share the same velocity and stress jump conditions as those in [29] for Stokes interface problems. Therefore, we only need to recall the CR- P_0 IFE shape functions constructed in [29]. To be more specific, a typical interface element $T \in \mathcal{T}_h^i$, can be classified into three types depending on the locations of the intersection points of the interface Γ and the edges of T as it is illustrated in Figure 3. Let D and E be the intersection points and let I be the line passing through D, E with the normal vector $\bar{\mathbf{n}} = (\bar{\mathbf{n}}_x, \bar{\mathbf{n}}_y)$, i.e., it is a linear approximation of the interface. The line I splits I into two subelements I_l^{\pm} . Thus, a vector-valued IFE shape function $\Phi_{i,T}(x,y)$ whose component is a piecewise linear or piecewise constant polynomial

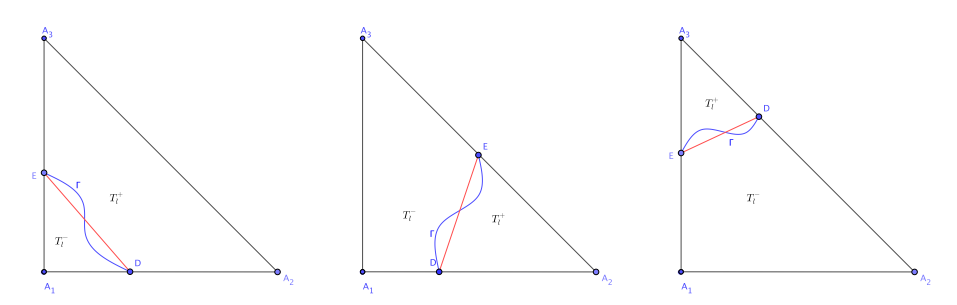


FIGURE 3. an interface element of Type I (left), Type II (middle) and Type III(right).

on an interface element $T \in \mathcal{T}_h^i$ is defined as follows [29]:

(9)

$$\phi_{i,T}(x,y) = \begin{cases} \phi_{i,T}^-(x,y) = \begin{bmatrix} \phi_{1,i}^-(x,y) \\ \phi_{2,i}^-(x,y) \\ \phi_{3,i}^-(x,y) \end{bmatrix} = \begin{bmatrix} a_{1,i}^-x + b_{1,i}^-y + c_{1,i}^- \\ a_{2,i}^-x + b_{2,i}^-y + c_{2,i}^- \\ d_i^- \end{bmatrix}, & \text{if } (x,y) \in T_l^-, \\ \phi_{1,i}^+(x,y) = \begin{bmatrix} \phi_{1,i}^+(x,y) \\ \phi_{2,i}^+(x,y) \\ \phi_{3,i}^+(x,y) \end{bmatrix} = \begin{bmatrix} a_{1,i}^+x + b_{1,i}^+y + c_{1,i}^+ \\ a_{2,i}^+x + b_{1,i}^+y + c_{1,i}^+ \\ a_{2,i}^+x + b_{2,i}^+y + c_{2,i}^+ \\ d_i^+ \end{bmatrix}, & \text{if } (x,y) \in T_l^+. \end{cases}$$

i = 1, 2, ... 7. The coefficients in (9) can be determined by the following conditions [29], for i = 1, 2, ..., 7:

• Six edge-valued conditions

(10)

$$\frac{1}{|e_j|} \int_{e_j} \phi_{i,T}(x,y) ds = \begin{bmatrix} \delta_{ij} \\ 0 \\ 0 \end{bmatrix}, \ j \in \mathcal{I}_T, \ \frac{1}{|e_{j-3}|} \int_{e_{j-3}} \phi_{i,T}(x,y) ds = \begin{bmatrix} 0 \\ \delta_{ij} \\ 0 \end{bmatrix}, \ j-3 \in \mathcal{I}_T.$$

• One mean pressure condition

(11)
$$\frac{1}{|T|} \int_{T} \phi_{i,T}(x,y) dX = \begin{bmatrix} 0 \\ 0 \\ \delta_{ij} \end{bmatrix}, \ j = 7.$$

• Four continuous conditions derived from (3a)

(12)
$$[\phi_{k,i}(D)] = [\phi_{k,i}(E)] = 0, \ k = 1, 2.$$

• Two stress continuous conditions derived from (3b)

(13)
$$[\mu \left(2\partial_x \phi_{1,i} \overline{\mathbf{n}}_x + (\partial_y \phi_{1,i} + \partial_x \phi_{2,i}) \overline{\mathbf{n}}_y\right) - \phi_{3,i} \overline{\mathbf{n}}_x]_{\overline{DE}} = 0,$$

$$[\mu \left((2\partial_x \phi_{2,i} + \partial_y \phi_{1,i}) \overline{\mathbf{n}}_x + 2\partial_y \phi_{2,i} \overline{\mathbf{n}}_y\right) - \phi_{3,i} \overline{\mathbf{n}}_y]_{\overline{DE}} = 0.$$

• One continuity of the divergence condition

$$[\partial_x \phi_{1,i} + \partial_y \phi_{2,i}]_{\overline{DE}} = 0.$$

As an illustration, we plot the three components of a CR- P_0 IFE shape function $\phi_{3,T}$ as well as the standard CR- P_0 FE shape function $\psi_{3,T}$ in Figure 4.

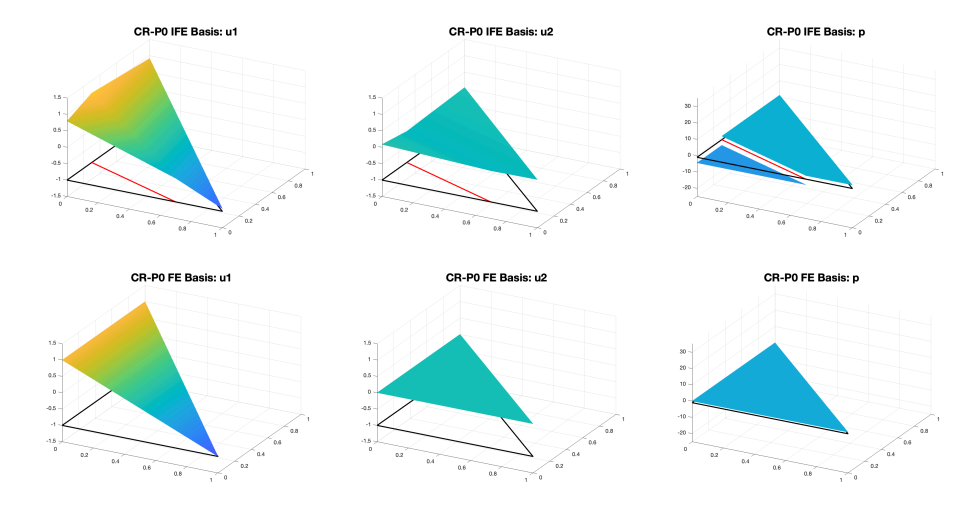


FIGURE 4. A comparison of a vector-valued IFE shape function $\phi_{3,T}$ (top) and the corresponding FE shape function $\psi_{3,T}$ (bottom) with $\mu^- = 10$ and $\mu^+ = 1$ on an interface triangle.

Therefore the local IFE space on the interface element is defined as $S_h^{int}(T) = \text{span}\{\phi_{i,T}, i=1,2,...,7\}$. As a result, the local IFE space can be summarized as:

(15)
$$\mathbf{S}_h(T) = \left\{ \begin{array}{l} \mathbf{S}_h^{non}(T), & \text{if } T \in \mathcal{T}_h^n, \\ \mathbf{S}_h^{int}(T), & \text{if } T \in \mathcal{T}_h^i. \end{array} \right.$$

We note that the unisolvency of the local $CR-P_0$ IFE space is guaranteed in Theorem 5.1 in [29]. Then the global $CR-P_0$ IFE space is defined as

(16)
$$\mathbf{S}_h(\Omega, \Gamma(t)) = \left\{ \mathbf{v} = [v_1, v_2, v_3]^t \in [L^2(\Omega)]^3 : \mathbf{v}|_T \in \mathbf{S}_h(T), \forall T \in \mathcal{T}_h, \right.$$
$$\operatorname{and} \int_e [v_i] ds = 0, \forall e \in \mathring{\mathcal{E}}_h, i = 1, 2 \right\}.$$

The corresponding subspace where the velocity vanishes on the boundary $\partial\Omega$ is defined as (17)

$$\boldsymbol{S}_h^0(\Omega,\Gamma(t)) = \left\{\boldsymbol{v} = [v_1,v_2,v_3]^t \in \boldsymbol{S}_h(\Omega,\Gamma(t)) : \int_e v_i ds = 0, \forall e \in \mathcal{E}_h^b, i = 1,2\right\}.$$

3. Nonconforming IFE methods

In this section, we derive the semi-discrete and full-discrete nonconforming IFE method for solving the unsteady NS interface problems in (1)-(3).

3.1. Weak formulation. We first derive the weak formulation of the NS interface problems. In the following, we use $(\cdot, \cdot)_{\omega}$ to denote the L^2 inner product on $\omega \subset \Omega$. For simplicity, we often drop the subscript if $\omega = \Omega$. For simplicity, we denote $\Omega^s(t)$ as Ω^s , $s = \pm$, in the deriviation. Given any time $t \in [0, T]$, multiplying (1a) by $\mathbf{v} \in [H_0^1(\Omega)]^2$ and using the Green's formula on Ω^- , it follows

$$(\boldsymbol{u}_{t}, \boldsymbol{v})_{\Omega^{-}} + ((2\mu\epsilon(\boldsymbol{u}) - p\boldsymbol{I}), \nabla \boldsymbol{v})_{\Omega^{-}} + ((\boldsymbol{u} \cdot \nabla)\boldsymbol{u}, \boldsymbol{v})_{\Omega^{-}} - ((2\mu\epsilon(\boldsymbol{u}) - p\boldsymbol{I})\mathbf{n}_{\partial\Omega^{-}}, \boldsymbol{v})_{\partial\Omega^{-}} = (\boldsymbol{f}, \boldsymbol{v})_{\Omega^{-}}.$$

Here, the second term is the inner product of two tensors $\mathbf{A} = [a_{ij}]$ and $\mathbf{B} = [b_{ij}]$, which is defined as $(\mathbf{A}, \mathbf{B}) = \sum_{i=1}^{n} \sum_{j=1}^{n} (a_{ij}, b_{ij})$. Note that $\mathbf{v}|_{\partial\Omega} = \mathbf{0}$ and \mathbf{n}_{Γ} points from Ω^{-} to Ω^{+} , then the above equation becomes

(18)
$$(\boldsymbol{u}_{t}, \boldsymbol{v})_{\Omega^{-}} + ((2\mu\epsilon(\boldsymbol{u}) - p\boldsymbol{I}), \nabla \boldsymbol{v})_{\Omega^{-}} + ((\boldsymbol{u} \cdot \nabla)\boldsymbol{u}, \boldsymbol{v})_{\Omega^{-}} - ((2\mu\epsilon(\boldsymbol{u}) - p\boldsymbol{I})\mathbf{n}_{\Gamma}, \boldsymbol{v})_{\Gamma} = (\boldsymbol{f}, \boldsymbol{v})_{\Omega^{-}}.$$

Similarly, on the subdomain Ω^+ we have

(19)
$$(\boldsymbol{u}_{t}, \boldsymbol{v})_{\Omega^{+}} + ((2\mu\epsilon(\boldsymbol{u}) - p\boldsymbol{I}), \nabla \boldsymbol{v})_{\Omega^{+}} + ((\boldsymbol{u} \cdot \nabla)\boldsymbol{u}, \boldsymbol{v})_{\Omega^{+}} - ((2\mu\epsilon(\boldsymbol{u}) - p\boldsymbol{I})\mathbf{n}_{\Gamma}, \boldsymbol{v})_{\Gamma} = (\boldsymbol{f}, \boldsymbol{v})_{\Omega^{+}}.$$

Adding (18) to (19) yields

$$(\boldsymbol{u}_t, \boldsymbol{v}) + (2\mu\epsilon(\boldsymbol{u}) - p\boldsymbol{I}), \nabla \boldsymbol{v}) + ((\boldsymbol{u} \cdot \nabla)\boldsymbol{u}, \boldsymbol{v}) - ((2\mu\epsilon(\boldsymbol{u}) - p\boldsymbol{I})\mathbf{n}_{\Gamma}, \boldsymbol{v})_{\Gamma} = (\boldsymbol{f}, \boldsymbol{v}).$$

Applying the jump condition (3b), it follows

$$(\boldsymbol{u}_t, \boldsymbol{v}) + (2\mu\epsilon(\boldsymbol{u}) - p\boldsymbol{I}), \nabla \boldsymbol{v}) + ((\boldsymbol{u} \cdot \nabla)\boldsymbol{u}, \boldsymbol{v}) = (\boldsymbol{f}, \boldsymbol{v}).$$

Using the identity $((2\mu\epsilon(\boldsymbol{u}) - p\boldsymbol{I}), \nabla \boldsymbol{v}) = (2\mu\epsilon(\boldsymbol{u}), \epsilon(\boldsymbol{v})) - (p, (\nabla \cdot \boldsymbol{v}))$ to rewrite the second term, we have

$$(\boldsymbol{u}_t, \boldsymbol{v}) + (2\mu\epsilon(\boldsymbol{u}), \epsilon(\boldsymbol{v})) - (p, (\nabla \cdot \boldsymbol{v})) + ((\boldsymbol{u} \cdot \nabla)\boldsymbol{u}, \boldsymbol{v}) = (\boldsymbol{f}, \boldsymbol{v}).$$

For the equation of incompressibility condition (1b), we multiply $q \in L^2(\Omega)$ on both sides and integrate over the domain Ω

$$(q, (\nabla \cdot \boldsymbol{u})) = 0.$$

The weak formulation of the NS interface problem is summarized as: find $(\boldsymbol{u}, p) \in H^1([0,T]; [H^1_0(\Omega)]^2 \times L^2(\Omega))$, such that for all $t \in [0,T]$ (20)

$$(\boldsymbol{u}_t, \boldsymbol{v}) + c(\boldsymbol{u}; \boldsymbol{u}, \boldsymbol{v}) + a(\boldsymbol{u}, \boldsymbol{v}) - b(\boldsymbol{v}, p) - b(\boldsymbol{u}, q) = L_{\boldsymbol{f}}(\boldsymbol{v}), \ \forall \boldsymbol{v} \in [H_0^1(\Omega)]^2, \ \forall q \in L^2(\Omega),$$

where the trilinear form $c(\cdot;\cdot,\cdot):[H_0^1(\Omega)]^2\times[H_0^1(\Omega)]^2\times[H_0^1(\Omega)]^2\to\mathbb{R}$ is defined as

$$c(\boldsymbol{u}; \boldsymbol{v}, \boldsymbol{w}) = ((\boldsymbol{u} \cdot \nabla) \boldsymbol{v} \cdot \boldsymbol{w}), \ \forall \boldsymbol{u}, \boldsymbol{v}, \boldsymbol{w} \in [H_0^1(\Omega)]^2,$$

the bilinear form $a(\cdot,\cdot):[H_0^1(\Omega)]^2\times[H_0^1(\Omega)]^2\to\mathbb{R}$ is defined as

$$a(\boldsymbol{u}, \boldsymbol{v}) = (2\mu\epsilon(\boldsymbol{u}), \epsilon(\boldsymbol{v})), \ \forall \boldsymbol{u}, \boldsymbol{v} \in [H_0^1(\Omega)]^2,$$

the bilinear form $b(\cdot,\cdot):[H_0^1(\Omega)]^2\times L^2(\Omega)\to\mathbb{R}$ is defined as

$$b(\boldsymbol{u},q) = (q,(\nabla \cdot \boldsymbol{u})), \ \forall \boldsymbol{u} \in [H_0^1(\Omega)]^2, q \in L^2(\Omega),$$

and the linear form $L_f(\cdot): [H_0^1(\Omega)]^2 \to \mathbb{R}$ is defined to be

$$L_{\mathbf{f}}(\mathbf{v}) = (\mathbf{f}, \mathbf{v}), \ \forall \mathbf{v} \in [H_0^1(\Omega)]^2.$$

3.2. Semi-discrete scheme. For spatial discretization, we use the CR- P_0 IFE space $S_h(\Omega,\Gamma(t))$ to replace the Sobolev space $[H_0^1(\Omega)]^2 \times L^2(\Omega)$ at the continuous level. Based on the weak formulation (20), we have the semi-discrete nonconforming CR- P_0 IFE methods for NS interface problem: find $(\boldsymbol{u}_h,p_h)\in H^1\left([0,T];\boldsymbol{S}_h(\Omega,\Gamma(t))\right)$ such that for $\forall t\in[0,T]$

$$(21)^{(\boldsymbol{u}_{h}, \boldsymbol{v}_{h}) + c(\boldsymbol{u}_{h}; \boldsymbol{u}_{h}, \boldsymbol{v}_{h}) + a(\boldsymbol{u}_{h}, \boldsymbol{v}_{h}) - b(\boldsymbol{v}_{h}, p_{h}) - b(\boldsymbol{u}_{h}, q_{h}) = L_{\boldsymbol{f}}(\boldsymbol{v}_{h}),}$$

$$\forall (\boldsymbol{v}_{h}, q_{h}) \in \boldsymbol{S}_{h}^{0}(\Omega, \Gamma(t)),$$

along with the initial conditions

(22)
$$u_h(\cdot,0) = u_{0,h}, \quad p_h(\cdot,0) = p_{0,h},$$

where $u_{0,h}$ and $p_{0,h}$ are some approximations, such as the interpolations, of u_0 and p_0 , respectively, in the IFE space $S_h(\Omega, \Gamma(t))$. We can rewrite the semi-discrete scheme (21)-(22) into the following **matrix form**: find U(t) such that

(23)
$$M(t)\mathbf{U}'(t) + N(\mathbf{U}(t)) + A(t)\mathbf{U}(t) = \mathbf{F}(t),$$
$$\mathbf{U}(0) = \mathbf{U}^{0},$$

where M(t) and A(t) are the IFE mass and stiffness matrices, respectively. These matrices are time-dependent [30] if the interface is moving (i.e. $\Gamma = \Gamma(t)$), because the set of interface elements \mathcal{T}_h^i and non-interface elements \mathcal{T}_h^n employed to formulate those two matrices are time-dependent. N(U(t)) corresponds to the nonlinear convective term $c(\boldsymbol{u}_h; \boldsymbol{u}_h, \boldsymbol{v}_h)$, and $\boldsymbol{F}(t)$ corresponds to the right-hand side of (21). Note that (23) is an initial-value problem of a nonlinear ordinary differential equation system for $\boldsymbol{U}(t)$ derived from the method of lines. We may use desired ODE solvers to solve this PDE induced ODE system [35].

Remark 3.1. For the steady-state NS interface problem, i.e., $\mathbf{u}(\mathbf{x},t) = \mathbf{u}(\mathbf{x})$, then $\mathbf{u}_t \equiv 0$ in (1a) and the initial conditions (1d) disappear. The CR-P₀ IFE method in (21) can still be employed by omitting the first term involving $\mathbf{u}_{h,t}$. In this case, appropriate techniques must be used to handle the nonlinear term, such as Newton's method. In the full-discrete scheme below, the Newton's method will be presented with more details.

3.3. Full-discrete scheme. To introduce the full-discrete scheme, we employ a uniform partition in time such that

$$\Pi_{\tau} = \{0 = t_0 < t_1 < \dots < t_{M-1} < t_M = T\},\$$

where $\tau = T/M$ and $t_n = t_0 + n\tau$, with $n = 0, 1, \dots, M$. For a function $\phi(\boldsymbol{x}, t)$, we denote $\phi(\boldsymbol{x}, t^n) = \phi^n(\boldsymbol{x})$, and introduce the backward difference operator $\overline{\partial}_t$ as follows

$$\overline{\partial}_t \phi^{n+1}(\boldsymbol{x}) = \frac{\phi^{n+1}(\boldsymbol{x}) - \phi^n(\boldsymbol{x})}{\tau}.$$

Then a full-discrete CR- P_0 IFE method (backward Euler scheme) can be described as: for each $n = 1, 2, \dots, M$, find $(\boldsymbol{u}_h^n, p_h^n) \subset \boldsymbol{S}_h(\Omega, \Gamma^n)$, such that

(24)

$$(\overline{\partial}_{t}\boldsymbol{u}_{h}^{n+1},\boldsymbol{v}_{h}^{n+1}) + c(\boldsymbol{u}_{h}^{n+1};\boldsymbol{u}_{h}^{n+1},\boldsymbol{v}_{h}^{n+1}) + a(\boldsymbol{u}_{h}^{n+1},\boldsymbol{v}_{h}^{n+1}) - b(\boldsymbol{v}_{h}^{n+1},p_{h}^{n+1}) - b(\boldsymbol{u}_{h}^{n+1},q_{h}^{n+1}) = L_{\boldsymbol{f}^{n+1}}(\boldsymbol{v}_{h}^{n+1}), \quad \forall (\boldsymbol{v}_{h}^{n+1},q_{h}^{n+1}) \in \boldsymbol{S}_{h}^{0}(\Omega,\Gamma^{n+1}).$$

That is

(25)

$$\begin{split} &\frac{1}{\tau}(\boldsymbol{u}_{h}^{n+1},\boldsymbol{v}_{h}^{n+1}) - \frac{1}{\tau}(\boldsymbol{u}_{h}^{n},\boldsymbol{v}_{h}^{n+1}) + c(\boldsymbol{u}_{h}^{n+1};\boldsymbol{u}_{h}^{n+1},\boldsymbol{v}_{h}^{n+1}) + a(\boldsymbol{u}_{h}^{n+1},\boldsymbol{v}_{h}^{n+1}) \\ &- b(\boldsymbol{v}_{h}^{n+1},p_{h}^{n+1}) - b(\boldsymbol{u}_{h}^{n+1},q_{h}^{n+1}) = L_{\boldsymbol{f}^{n+1}}(\boldsymbol{v}_{h}^{n+1}), \quad \forall (\boldsymbol{v}_{h}^{n+1},q_{h}^{n+1}) \in \boldsymbol{S}_{h}^{0}(\Omega,\Gamma^{n+1}). \end{split}$$

Note that in the second term of (25), \boldsymbol{u}_h^n , and \boldsymbol{v}_h^{n+1} are at two different time levels which correspond two interface locations Γ^n and Γ^{n+1} . To avoid handling two interfaces, we replace \boldsymbol{v}_h^{n+1} with \boldsymbol{v}_h^n . This technique was used in [25]. Then it follows

(26)

$$\begin{split} &\frac{1}{\tau}(\boldsymbol{u}_h^{n+1}, \boldsymbol{v}_h^{n+1}) - \frac{1}{\tau}(\boldsymbol{u}_h^{n}, \boldsymbol{v}_h^{n}) + c(\boldsymbol{u}_h^{n+1}; \boldsymbol{u}_h^{n+1}, \boldsymbol{v}_h^{n+1}) + a(\boldsymbol{u}_h^{n+1}, \boldsymbol{v}_h^{n+1}) \\ &- b(\boldsymbol{v}_h^{n+1}, p_h^{n+1}) - b(\boldsymbol{u}_h^{n+1}, q_h^{n+1}) = L_{\boldsymbol{f}^{n+1}}(\boldsymbol{v}_h^{n+1}), \quad \forall (\boldsymbol{v}_h^{n+1}, q_h^{n+1}) \in \boldsymbol{S}_h^0(\Omega, \Gamma^{n+1}), \end{split}$$

with the initial conditions

(27)
$$\mathbf{u}_h^0 = \mathbf{u}_{0,h}, \quad p_h^0 = p_{0,h},$$

where $\Gamma^n = \Gamma(t_n)$. The following Newton's iteration is used to handle the nonlinear convective term $c(\boldsymbol{u}_h^{n+1}; \boldsymbol{u}_h^{n+1}, \boldsymbol{v}_h)$: find $(\boldsymbol{u}_h^{n,(l)}, p_h^{n,(l)}) \subset \boldsymbol{S}_h(\Omega, \Gamma^n)$, $l \in \mathbb{N}^+$, such that

$$\frac{1}{\tau}(\boldsymbol{u}_{h}^{n+1,(l)}, \boldsymbol{v}_{h}^{n+1}) - \frac{1}{\tau}(\boldsymbol{u}_{h}^{n,(l)}, \boldsymbol{v}_{h}^{n}) + c(\boldsymbol{u}_{h}^{n+1,(l)}; \boldsymbol{u}_{h}^{n+1,(l-1)}, \boldsymbol{v}_{h}^{n+1}) \\
+ c(\boldsymbol{u}_{h}^{n+1,(l-1)}; \boldsymbol{u}_{h}^{n+1,(l)}, \boldsymbol{v}_{h}^{n+1}) + a(\boldsymbol{u}_{h}^{n+1,(l)}, \boldsymbol{v}_{h}^{n+1}) \\
- b(\boldsymbol{v}_{h}^{n+1}, p_{h}^{n+1,(l)}) - b(\boldsymbol{u}_{h}^{n+1,(l)}, q_{h}^{n+1}) \\
= L_{\boldsymbol{f}^{n+1}}(\boldsymbol{v}_{h}^{n+1}) + c(\boldsymbol{u}_{h}^{n+1,(l-1)}; \boldsymbol{u}_{h}^{n+1,(l-1)}, \boldsymbol{v}_{h}^{n+1}), \\
\forall (\boldsymbol{v}_{h}^{n+1}, q_{h}^{n+1}) \in \boldsymbol{S}_{h}^{0}(\Omega, \Gamma^{n+1}),$$

with the initial conditions

(29)
$$u_h^{0,(0)} = u_{0,h}, \quad p_h^{0,(0)} = p_{0,h}.$$

At each time level, the initial guess is chosen as the solution from the previous time level, i.e.,

(30)
$$\boldsymbol{u}_{h}^{n+1,(0)} = \boldsymbol{u}_{h}^{n,(l)}, \quad p_{h}^{n+1,(0)} = p_{h}^{n,(l)}.$$

In the actual computation, the stopping criteria for the Newton's method in (28) is regulated by

(31)
$$\sqrt{\|\boldsymbol{u}_{h}^{n,(l)} - \boldsymbol{u}_{h}^{n,(l-1)}\|_{L^{2}(\Omega)}^{2} + \|\boldsymbol{p}_{h}^{n,(l)} - \boldsymbol{p}_{h}^{n,(l-1)}\|_{L^{2}(\Omega)}^{2}} < \epsilon_{0},$$

for some prescribed threshold $\epsilon_0 > 0$.

Next, we derive the matrix form of the backward Euler scheme. Let $t=t_{n+1}$ in (23), then

(32)
$$M(t_{n+1})U'(t_{n+1}) + N(U(t_{n+1})) + A(t_{n+1})U(t_{n+1}) = F(t_{n+1}).$$

Applying the backward Euler scheme to the above equation and utilizing

$$M(t_{n+1})U'(t_{n+1}) \approx (M(t_{n+1})U(t_{n+1}) - M(t_n)U(t_n))/\tau$$

which leads to

(33)
$$\left(\frac{1}{\tau}M(t_{n+1}) + A(t_{n+1})\right) \boldsymbol{U}^{n+1} + N(\boldsymbol{U}^{n+1}) = \frac{1}{\tau}M(t_n)\boldsymbol{U}^n + \boldsymbol{F}^{n+1}.$$

Here and thereafter, we use more compact notations $A^{n+1} = A(t_{n+1})$, $M^{n+1} = M(t_{n+1})$, $\boldsymbol{U}^{n+1} = \boldsymbol{U}(t_{n+1})$ and $\boldsymbol{F}^{n+1} = \boldsymbol{F}(t_{n+1})$ as above.

Applying the Newton's method in (28) to (33), we have the following **matrix form** of the backward Euler scheme with Newton's method: find a sequence $\{U^{n+1,(l)}\}_{n=0}^{M}$ such that

(34)
$$\begin{pmatrix} \frac{1}{\tau} M^{n+1} + A^{n+1} + N_1(\boldsymbol{U}^{n+1,(l-1)}) + N_2(\boldsymbol{U}^{n+1,(l-1)}) \end{pmatrix} \boldsymbol{U}^{n+1,(l)}$$
$$= \frac{1}{\tau} M^n \boldsymbol{U}^n + \boldsymbol{F}^{n+1} + \boldsymbol{F}_N^{n+1,(l-1)},$$

with the initial condition

$$(35) U^{0,(l)} = U^0.$$

Here, given the function $\boldsymbol{u}_h^{n+1,(l-1)}$, the matrix $N_1(\boldsymbol{U}^{n+1,(l-1)})$ corresponds to the bilinear form $c(\cdot;\boldsymbol{u}_h^{n+1,(l-1)},\cdot)$, and the matrix $N_2(\boldsymbol{U}^{n+1,(l-1)})$ corresponds to the bilinear form $c(\boldsymbol{u}_h^{n+1,(l-1)};\cdot,\cdot)$. The vector $\boldsymbol{F}_N^{n+1,(l-1)}$ is associated with the linear form $c(\boldsymbol{u}_h^{n+1,(l-1)};\boldsymbol{u}_h^{n+1,(l-1)},\cdot)$. Setting the stopping criteria to be

(36)
$$\|\boldsymbol{U}^{n+1,(l)} - \boldsymbol{U}^{n+1,(l-1)}\| < \epsilon_0,$$

we can summarize our full-discrete backward Euler IFE scheme with Newton's iterations in the following algorithm.

Algorithm 1 Backward Euler IFE scheme with Newton's iteration

```
Step 1: Compute \mathbf{U}_0 form initial condition, and let \boldsymbol{U}^{1,(0)} \leftarrow \boldsymbol{U}^0.

Step 2: For n=0,1,\cdots,N-1, compute the global vector \boldsymbol{F}^{n+1}. Compute the global IFE matrices M^{n+1}, A^{n+1} and M^n. Let l=0.

Step 3: While l=0 or \|\boldsymbol{U}^{n+1,(l)}-\boldsymbol{U}^{n+1,(l-1)}\|>\epsilon_0

Step 4: compute N_1(\boldsymbol{U}^{n+1,(l-1)}) and N_2(\boldsymbol{U}^{n+1,(l-1)}), and \boldsymbol{F}_N^{n+1,(l-1)}
```

Step 5: solve $U^{n+1,(l)}$ from (34). Step 6: $l \leftarrow l+1$, return to Step 4.

Step 7: Set $n \leftarrow n+1$, and $\boldsymbol{U}^{n+1,(0)} \leftarrow \boldsymbol{U}^{n,(l)} = \boldsymbol{U}^n$

End

Remark 3.2. In the case that the viscosity coefficient function μ is time-independent as stated in (2) and the interface is stationary, we only need to compute the global matrices M and A associated with linear terms once. The global vector for linear terms \mathbf{F}^{n+1} must be updated in each time iteration. The global matrices associated with the nonlinear terms $N_1(\mathbf{U}^{n+1,(l-1)})$ and $N_2(\mathbf{U}^{n+1,(l-1)})$ and the nonlinear global vector $\mathbf{F}_N^{n+1,(l-1)}$ must be updated at each time step and each Newton's iteration.

Remark 3.3. If the viscosity coefficient function μ is time-dependent, i.e., $\mu = \mu(\mathbf{x}, t)$ but the interface is stationary, then the stiffness matrix A also depends on time, and it must be updated in each time iteration. However, the mass matrix remains time independent. In this case, (34) becomes

$$\left(\frac{1}{\tau}M + A^{n+1} + N_1(\boldsymbol{U}^{n+1,(l-1)}) + N_2(\boldsymbol{U}^{n+1,(l-1)})\right)\boldsymbol{U}^{n+1,(l)}$$

$$= \frac{1}{\tau}M\boldsymbol{U}^n + \boldsymbol{F}^{n+1} + \boldsymbol{F}_N^{n+1,(l-1)}.$$
(37)

Remark 3.4. For moving interface problems, the assembly of global matrices A^{n+1} , M^{n+1} in (34) only requires updating local matrices on those elements where the interface configuration changes during the two consecutive time steps. This feature enables fast assembly of global matrices for moving interface problems due to the isomorphism of our IFE spaces with standard FE spaces.

4. Numerical Examples

In this section, we test the performance of the nonconforming $CR-P_0$ IFE method for the NS interface problem (1)-(3) through a sequence of numerical experiments, with different values of jumps in viscosity coefficients and interface configurations. Errors of the nonconforming IFE solutions for the velocity and the pressure are

measured by the L^2 norm and the broken H^1 semi-norms. We introduce the following notations to measure the errors of IFE solutions and the convergence rates: let $\boldsymbol{u}=(u_1,u_2)^t$ and p be the exact solution of (1) and let $\boldsymbol{u}_h=(u_{1,h},u_{2,h})^t$ and p_h be the nonconforming IFE solutions of (24). Then the errors of the IFE solutions are denoted as

$$e_{1,h} = u_1 - u_{1,h}, \ e_{2,h} = u_2 - u_{2,h}, \ e_{3,h} = p - p_h.$$

The rate of convergence r is computed via two consecutive meshes \mathcal{T}_{h_1} and \mathcal{T}_{h_2} with

$$r = \frac{\log(\|e_{h_1}\|/\|e_{h_2}\|)}{\log(h_1/h_2)},$$

where $\|\cdot\|$ is either L^2 norm or the broken H^1 semi-norm.

Let the computational domain be $\Omega = [-1, 1] \times [-1, 1]$. A Cartesian triangular mesh \mathcal{T}_h of Ω is generated by partitioning Ω into $N \times N$ congruent squares with the side length h = 2/N, and then partitioning each square into two congruent triangles by its diagonal line.

Example 1. (Steady-state NSE with linear interface) In this example, we consider the IFE method for a steady-state NS interface problem. The interface Γ is a straight line: $\Gamma = \{(x,y) : y = 0\}$, splitting the domain into two subdomains $\Omega^- = \{(x,y) : y < 0\}$ and $\Omega^+ = \{(x,y) : y > 0\}$. The exact solution \mathbf{u} and p are given by

$$(38) \quad \boldsymbol{u}(x,y) = \begin{cases} u_1(x,y) = \begin{cases} \frac{1}{\mu^-} \sin^2(\pi x) \sin(\pi y) \cos(\pi y), & \text{if } (x,y) \in \Omega^-, \\ \frac{1}{\mu^+} \sin^2(\pi x) \sin(\pi y) \cos(\pi y), & \text{if } (x,y) \in \Omega^+, \\ u_2(x,y) = \begin{cases} -\frac{1}{\mu^-} \sin^2(\pi y) \sin(\pi x) \cos(\pi x), & \text{if } (x,y) \in \Omega^-, \\ -\frac{1}{\mu^+} \sin^2(\pi y) \sin(\pi x) \cos(\pi x), & \text{if } (x,y) \in \Omega^+, \end{cases}$$

(39)
$$p(x,y) = -\frac{1}{4}\sin(\pi x)\sin(\pi y)\left(\cos(2\pi x) + \cos(2\pi y)\right),$$

which shares some similarities to a Taylor-Green vortex (although the arrangement of the velocity pattern is different, as shown in Figure 6). The viscosity coefficient is chosen to be $(\mu^-, \mu^+) = (1, 2.5)$.

For steady-state NS interface problems, as stated in Remark 3.1, the IFE solutions are generated by (21) (omitting the term involving $u_{h,t}$) combined with the Newton's method in Algorithm 1. We note that only Steps 3-7 are employed and all superscripts with respect to the time levels n or n+1 should be omitted, thus the output IFE solution is $\boldsymbol{U}^{(l)}$.

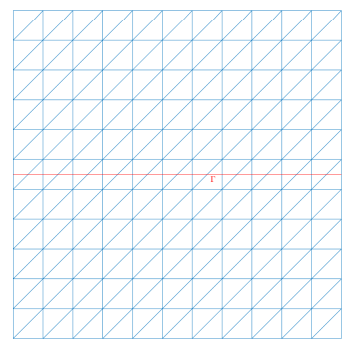
In Table 1, we report the errors and the convergence rates of the CR- P_0 IFE solutions. Note that these numerical results are obtained on a sequence of interface-unfitted meshes where the interface intersects with the interior of some of the elements (an illustration of such an interface-unfitted mesh is sketched in the left subfigure of Figure 5). In our computation, It takes no more than four iterations for the Newton's method to converge within the threshold $\epsilon_0 = 10^{-6}$ in (31). It can be seen that the convergence rates for velocity components u_1 and u_2 approach to $O(h^2)$ in the L^2 norm and O(h) in the H^1 semi-norm; convergence rates for the pressure p approach to O(h) in the L^2 norm as the mesh becomes finer. These results demonstrate the optimal orders of convergence, which are consistent with our expectation according to the degrees of polynomials employed for the approximation. In Table 3, we present the errors and the convergence rates of the finite element methods solutions obtained on body-fitting meshes (where the mesh is

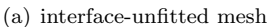
Table 1. Errors of IFE solutions for Example 2, $(\mu^-, \mu^+) = (1, 2.5)$.

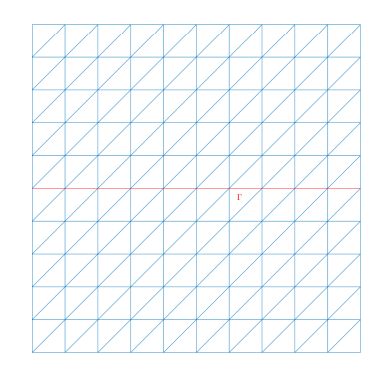
N	$ e_{1,h} _{0,\Omega}$	r	$ e_{2,h} _{0,\Omega}$	r	$ e_{3,h} _{0,\Omega}$	r	$ e_1 _{1,\Omega}$	r	$ e_{2} _{1,\Omega}$	r
11	3.41e-02	NA	3.32e-02	NA	3.98e-01	NA	8.99e-01	NA	8.94e-01	NA
21	9.85e-03	1.86	9.65e-03	1.85	2.06e-01	0.98	4.81e-01	0.94	4.80e-01	0.93
41	2.63e-03	1.94	2.58e-03	1.94	1.03e-01	1.01	2.48e-01	0.97	2.48e-01	0.97
81	6.78e-04	1.97	6.66e-04	1.97	5.18e-02	1.01	1.26e-01	0.99	1.26e-01	0.99
161	1.72e-04	1.99	1.69e-04	1.99	2.59e-02	1.00	6.33e-02	0.99	6.33e-02	0.99
321	4.32e-05	2.00	4.25e-05	2.00	1.30e-02	1.00	3.18e-02	1.00	3.18e-02	1.00

TABLE 2. Errors of FE solutions on body-fitting meshes for Example 2, $(\mu^-, \mu^+) = (1, 2.5)$.

N	$ e_{1,h} _{0,\Omega}$	r	$ e_{2,h} _{0,\Omega}$	r	$ e_{3,h} _{0,\Omega}$	r	$ e_1 _{1,\Omega}$	r	$ e_2 _{1,\Omega}$	r
10	4.06e-02	NA	4.07e-02	NA	4.06e-01	NA	9.84e-01	NA	9.84e-01	NA
20	1.08e-02	1.91	1.08e-02	1.91	2.09e-01	0.96	5.05e-01	0.96	5.05e-01	0.96
40	2.76e-03	1.97	2.75e-03	1.97	1.04e-01	1.01	2.54e-01	0.99	2.54e-01	0.99
80	6.93e-04	1.99	6.91e-04	1.99	5.19e-02	1.00	1.27e-01	1.00	1.27e-01	1.00
160	1.74e-04	2.00	1.73e-04	2.00	2.59e-02	1.00	6.37e-02	1.00	6.37e-02	1.00
320	4.34e-05	2.00	4.32e-05	2.00	1.30e-02	1.00	3.19e-02	1.00	3.19e-02	1.00







(b) body-fitting mesh

FIGURE 5. interface-unfitted mesh (N=11) and body-fitting mesh (N=10) for Example 2.

aligned with the interface by configuration, an illustration of such a body-fitting mesh is sketched in the right subfigure of Figure 5), the rates of convergence are optimal as expected. Comparing data in Table 1 and Table 3, as well as the two velocity plots in Figure 6, it can be seen that the accuracy of IFE approximation on interface-unfitted meshes and FE approximation on body-fitting meshes are much alike.

Example 2. In this example, we consider a NS interface problem described by (1), where the interface Γ is a straight line: $\Gamma = \{(x,y) : y - \sqrt{0.3} = 0\}$. Then the interface Γ splits the domain into two subdomains $\Omega^- = \{(x,y) : y - \sqrt{0.3} < 0\}$ and $\Omega^+ = \{(x,y) : y - \sqrt{0.3} > 0\}$. The function \mathbf{f} in (1a) is generated with the following exact solution \mathbf{u} and \mathbf{p} :

(40)
$$\mathbf{u}(x,y) = \begin{cases} u_1(x,y) = \begin{cases} \frac{1}{\mu^-} (y - \sqrt{0.3}) x^2, & \text{if } (x,y) \in \Omega^-, \\ \frac{1}{\mu^+} (y - \sqrt{0.3}) x^2, & \text{if } (x,y) \in \Omega^+, \\ -\frac{1}{\mu^-} x (y - \sqrt{0.3})^2, & \text{if } (x,y) \in \Omega^-, \\ -\frac{1}{\mu^+} x (y - \sqrt{0.3})^2, & \text{if } (x,y) \in \Omega^+, \end{cases}$$

$$(41) p(x,y) = e^x - e^y.$$

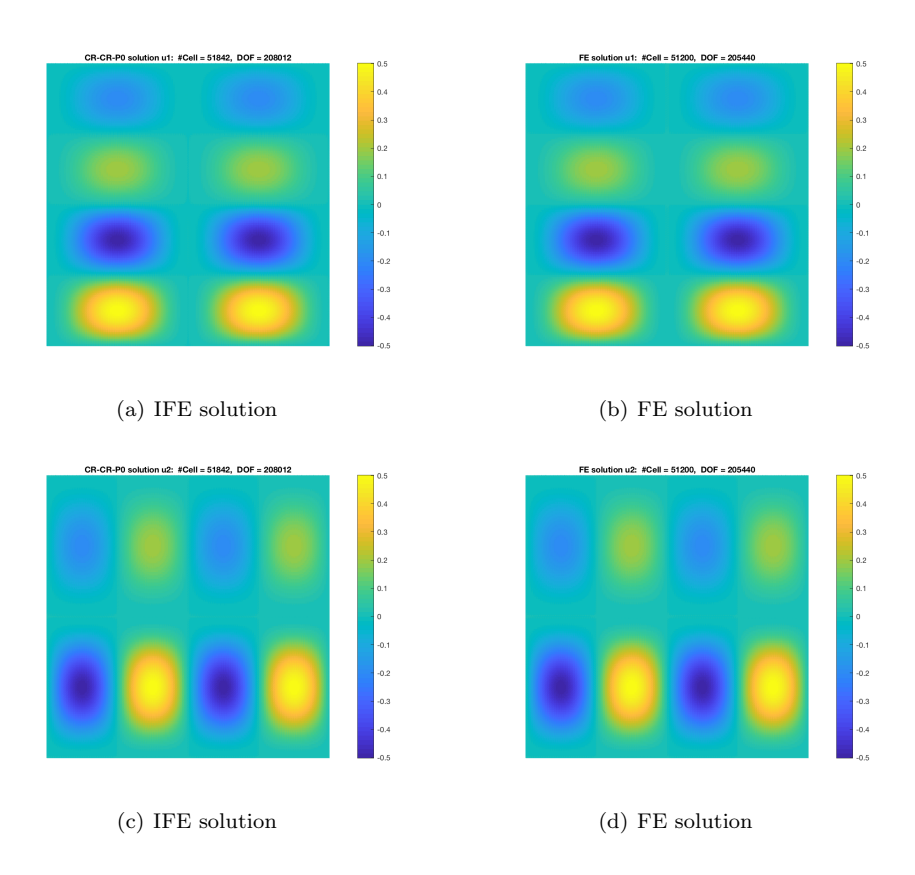


FIGURE 6. $u_{i,h}$ (IFE) with N = 161 and $u_{i,h}$ (FE) with N = 160 when $\mu^- = 1$, $\mu^+ = 2.5$. (i = 1, 2. Top plots: $u_{1,h}$; bottom: $u_{2,h}$).

In Table 3 and 4, we present the errors and the convergence rates of the CR- P_0 IFE solutions when the jump in viscosity coefficient is modest $(\mu^-, \mu^+) = (1, 10)$ and relatively large $(\mu^-, \mu^+) = (1, 1000)$, respectively. It takes about 3 Newton's iterations for the IFE methods to converge. It can be seen that the convergence rates for velocity components u_1 and u_2 approach to $O(h^2)$ in the L_2 norm and O(h) in the H^1 semi-norm; convergence rates for the pressure p approach to O(h) in the L_2 norm as the mesh becomes finer. These results demonstrate the optimal orders of convergence, which are consistent with our expectation according to the degrees of polynomials employed for the approximation.

Table 3. Errors of the IFE solutions for Examples 2, $(\mu^-, \mu^+) = (1, 10)$.

N	$ e_{1,h} _{0,\Omega}$	r	$ e_{2,h} _{0,\Omega}$	r	$ e_{3,h} _{0,\Omega}$	г	$ e_1 _{1,\Omega}$	r	$ e_{2} _{1,\Omega}$	r
10	1.67e-02	NA	1.30e-02	NA	2.82e-01	NA	2.82e-01	NA	2.54e-01	NA
20	4.78e-03	1.81	3.55e-03	1.87	1.19e-01	1.24	1.44e-01	0.97	1.29e-01	0.98
40	1.07e-03	2.15	8.70e-04	2.03	5.04e-02	1.25	7.15e-02	1.00	6.46e-02	1.00
80	2.70e-04	1.99	2.19e-04	1.99	2.50e-02	1.01	3.58e-02	1.00	3.24e-02	1.00
160	6.83e-05	1.98	5.48e-05	1.99	1.25e-02	1.00	1.79e-02	1.00	1.62e-02	1.00
320	1.82e-05	1.90	1.41e-05	1.96	6.61e-03	0.92	8.99e-03	1.00	8.11e-03	1.00

Example 3. (Steady-state NSE with a circular interface) In this example, we consider a steady-state NSE with a circular interface $\Gamma = \{(x,y) : x^2 + y^2 - 0.3 = 0\}$. The interface Γ splits the domain Ω into two subdomains: $\Omega^- = \{(x,y) : x^2 + y^2 - 0.3 = 0\}$.

TABLE 4. Errors of the IFE solutions for Examples 2, $(\mu^-, \mu^+) = (1, 1000)$.

N	$ e_{1,h} _{0,\Omega}$	r	$ e_{2,h} _{0,\Omega}$	r	$ e_{3,h} _{0,\Omega}$	г	$ e_1 _{1,\Omega}$	r	$ e_{2} _{1,\Omega}$	r
10	2.53e-02	NA	1.76e-02	NA	4.31e+00	NA	3.38e-01	NA	2.58e-01	NA
20	5.13e-03	2.31	3.66e-03	2.26	6.49e-01	2.73	1.56e-01	1.11	1.29e-01	1.00
40	1.12e-03	2.20	8.81e-04	2.05	1.04e + 00	-0.68	7.17e-02	1.12	6.46e-02	1.00
80	2.87e-04	1.96	2.25e-04	1.97	6.41e-01	0.70	3.59e-02	1.00	3.23e-02	1.00
160	7.45e-05	1.95	5.82e-05	1.95	3.35e-01	0.93	1.80e-02	1.00	1.62e-02	1.00
320	2.12e-05	1.81	1.57e-05	1.89	1.23e-01	1.44	9.39e-03	0.94	8.10e-03	1.00

 $x^2 + y^2 - 0.3 < 0$ and $\Omega^+ = \{(x,y) : x^2 + y^2 - 0.3 > 0\}$. The right hand side function \boldsymbol{f} in (1a) is generated with the following exact solution \boldsymbol{u} and p:

(42)
$$\mathbf{u}(x,y) = \begin{cases} u_1(x,y) = \begin{cases} \frac{1}{\mu^-} y(x^2 + y^2 - 0.3), & \text{if } (x,y) \in \Omega^-, \\ \frac{1}{\mu^+} y(x^2 + y^2 - 0.3), & \text{if } (x,y) \in \Omega^+, \\ -\frac{1}{\mu^-} x(x^2 + y^2 - 0.3), & \text{if } (x,y) \in \Omega^-, \\ -\frac{1}{\mu^+} x(x^2 + y^2 - 0.3), & \text{if } (x,y) \in \Omega^+, \end{cases}$$

(43)
$$p(x,y) = \frac{1}{10}(x^3 - y^3).$$

TABLE 5. Errors of IFE solutions for Example 3 with $(\mu^-, \mu^+) = (1, 10)$.

N	$ e_{1,h} _{0,\Omega}$	r	$ e_{2,h} _{0,\Omega}$	r	$ e_{3,h} _{0,\Omega}$	r	$ e_1 _{1,\Omega}$	r	$ e_{2} _{1,\Omega}$	r
10	4.59e-03	NA	4.58e-03	NA	1.12e-01	NA	1.02e-01	NA	1.02e-01	NA
20	1.20e-03	1.93	1.20e-03	1.93	3.98e-02	1.50	5.32e-02	0.93	5.33e-02	0.93
40	3.09e-04	1.96	3.09e-04	1.96	1.94e-02	1.03	2.75e-02	0.95	2.75e-02	0.96
80	7.89e-05	1.97	7.88e-05	1.97	8.52e-03	1.19	1.41e-02	0.96	1.40e-02	0.97
160	1.98e-05	2.00	1.98e-05	2.00	3.96e-03	1.11	7.04e-03	1.01	6.98e-03	1.01
320	4.97e-06	1.99	4.96e-06	1.99	1.86e-03	1.09	3.50e-03	1.01	3.48e-03	1.00

Table 6. Errors of IFE solutions for Example 3 with $(\mu^-, \mu^+) = (1, 1000)$.

N	$ e_{1,h} _{0,\Omega}$	r	$ e_{2,h} _{0,\Omega}$	r	$ e_{3,h} _{0,\Omega}$	r	$ e_1 _{1,\Omega}$	r	$ e_{2} _{1,\Omega}$	r
10	1.36e-02	NA	1.36e-02	NA	1.34e + 00	NA	1.48e-01	NA	1.48e-01	NA
20	3.08e-03	2.14	3.08e-03	2.14	1.40e + 00	-0.07	6.26e-02	1.24	6.28e-02	1.24
40	7.74e-04	1.99	7.74e-04	1.99	8.08e-01	0.79	2.80e-02	1.16	2.90e-02	1.17
80	1.43e-04	2.44	1.43e-04	2.44	3.04e-01	1.41	1.34e-02	1.06	1.33e-02	1.08
160	2.67e-05	2.42	2.67e-05	2.42	1.12e-01	1.45	6.57e-03	1.03	6.50e-03	1.03
320	5.32e-06	2.32	5.32e-06	2.32	3.99e-02	1.49	3.24e-03	1.02	3.22e-03	1.01

In Tables 5 and 6, we present the errors and the convergence rates of the CR- P_0 IFE solutions when the jump in viscosity coefficient is modest $(\mu^-, \mu^+) = (1, 10)$ and relatively large $(\mu^-, \mu^+) = (1, 1000)$, respectively. It takes about three iterations for the Newton's methods to converge below the threshold $\epsilon_0 = 10^{-6}$. It can also be seen that, even for the high-contrast viscosity coefficients, the convergence rates for the velocity components u_1 and u_2 approach to $O(h^2)$ in the L^2 norm and O(h) in the H^1 semi-norm; convergence rates for the pressure p approach to O(h) in the L^2 norm as the mesh becomes finer, which demonstrates the optimal rates of convergence of the IFE solutions.

We plot the numerical solutions and exact solutions when the contrast of the viscosity coefficients is $(\mu^-, \mu^+) = (1, 10)$ in Figure 7 with the division of the domain N=160. According to those graphs, the numerical solutions simulate the exact solution well and the numerical solutions are resolved accurately around the interface.

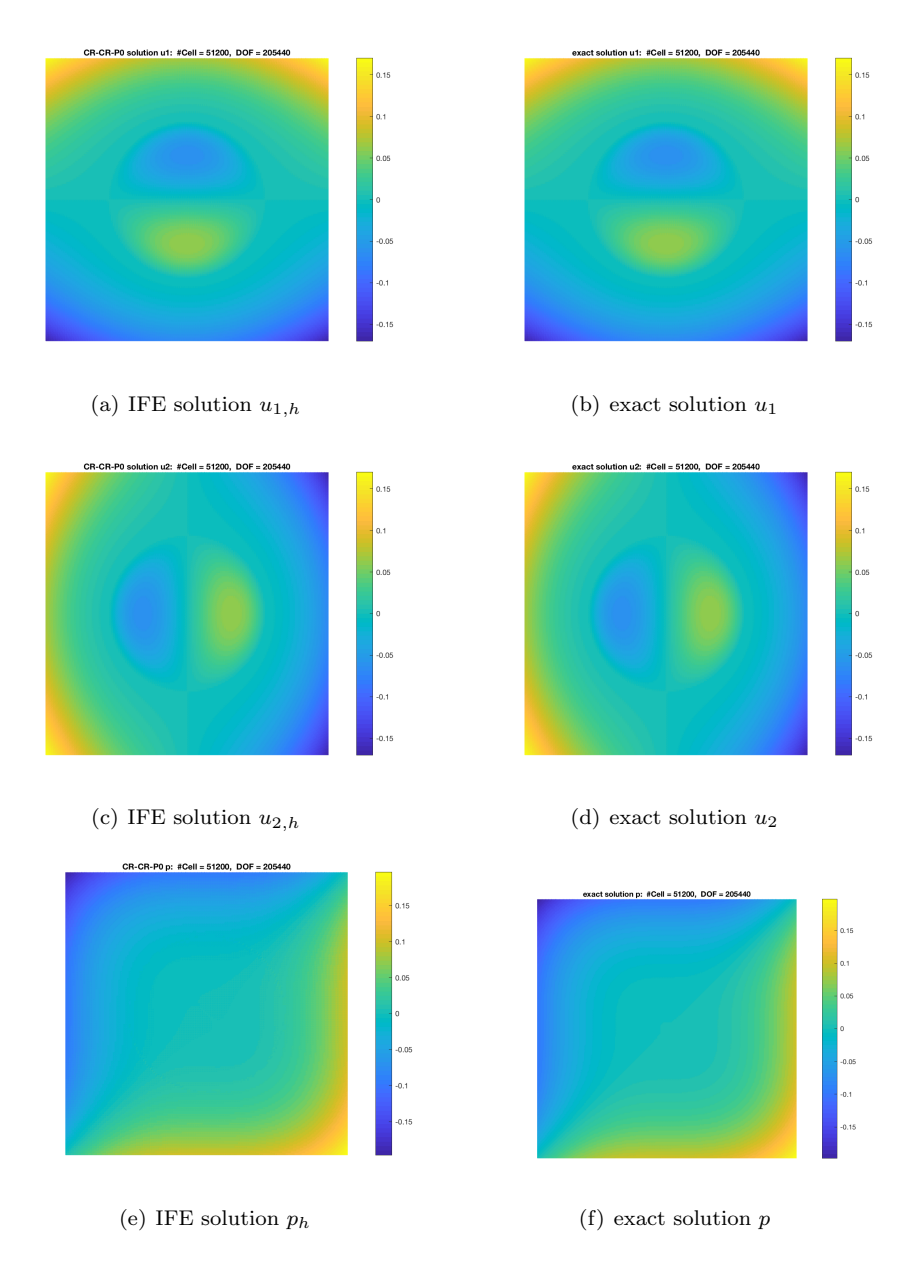


FIGURE 7. CR- P_0 IFE solution and exact solution (top to bottom: $u_1,\ u_2,\ p$) when $\mu^-=1,\ \mu^+=10,\ N=160.$

Example 4. (Unsteady NSE with a circular interface) In this example, we consider a time-dependent NS interface problem described by (1), with T=1. The circular interface: $\Gamma = \{(x,y): x^2+y^2-0.3=0\}$ splits the domain Ω into two subdomains: $\Omega^- = \{(x,y): x^2+y^2-0.3<0\}$ and $\Omega^+ = \{(x,y): x^2+y^2-0.3>0\}$.

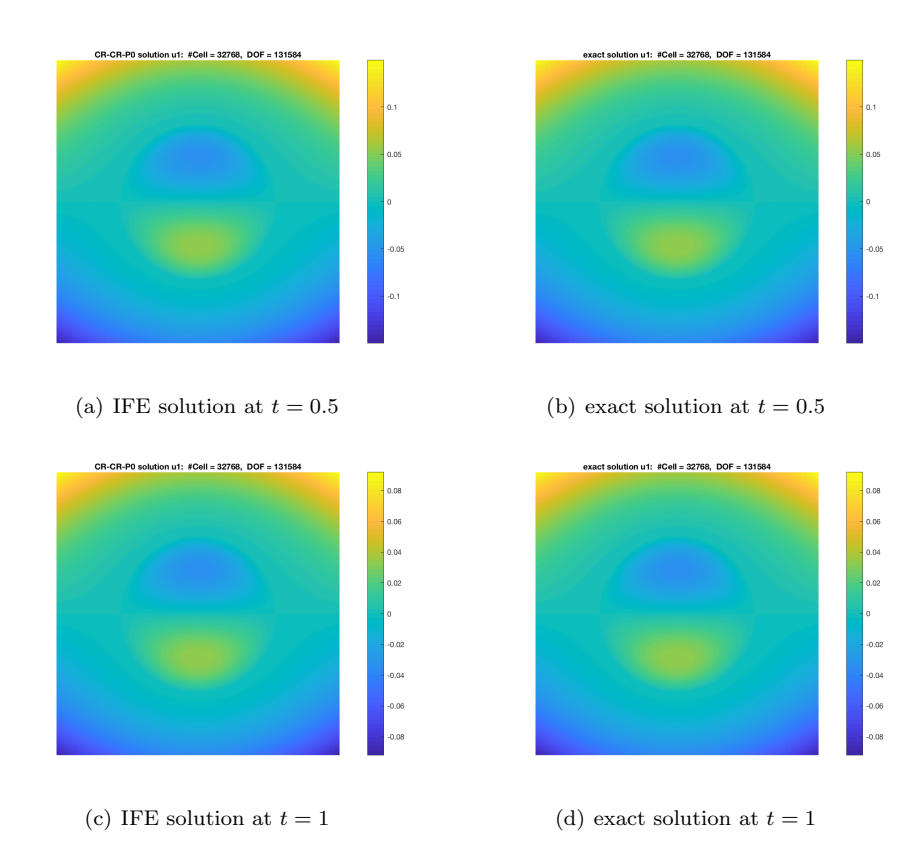


FIGURE 8. CR- P_0 IFE solution $u_{1,h}$ and exact solution u_1 at t=0.5 and t=1, when $\mu^-=1$, $\mu^+=10$, N=128.

The function f in (1a) is generated with the following exact solution u and p: (44)

$$\boldsymbol{u}(x,y,t) = \begin{cases} u_1(x,y,t) = \begin{cases} \frac{1}{\mu^-}y(x^2+y^2-0.3)\cos(t), & \text{if } (x,y) \in \Omega^-, \\ \frac{1}{\mu^+}y(x^2+y^2-0.3)\cos(t), & \text{if } (x,y) \in \Omega^+, \\ -\frac{1}{\mu^-}x(x^2+y^2-0.3)\cos(t), & \text{if } (x,y) \in \Omega^-, \\ -\frac{1}{\mu^+}x(x^2+y^2-0.3)\cos(t), & \text{if } (x,y) \in \Omega^+, \end{cases}$$

(45)
$$p(x,y) = \frac{1}{10}(x^3 - y^3).$$

The IFE solutions are generated using the backward Euler scheme described in (28), with the division of the time interval $M = N^2/8$.

Table 7. Errors of IFE solutions for Example 4 at t=1 with $\mu^-=1,\,\mu^+=10.$

N	$ e_{1,h} _{0,\Omega}$	r	$ e_{2,h} _{0,\Omega}$	r	$ e_{3,h} _{0,\Omega}$	r	$ e_1 _{1,\Omega}$	r	$ e_{2} _{1,\Omega}$	r
8	3.36e-03	NA	3.35e-03	NA	5.14e-02	NA	6.94e-02	NA	6.87e-02	NA
16	9.08e-04	1.89	9.08e-04	1.88	3.29e-02	0.65	3.57e-02	0.96	3.53e-02	0.96
32	2.40e-04	1.92	2.40e-04	1.92	1.50e-02	1.13	1.81e-02	0.98	1.81e-02	0.96
64	6.12e-05	1.97	6.12e-05	1.97	5.75e-03	1.38	9.23e-03	0.97	9.23e-03	0.97
128	1.52e-05	2.01	1.52e-05	2.01	2.66e-03	1.11	4.68e-03	0.98	4.67e-03	0.98

TABLE 8. Errors of IFE solutions for Example 4 at t=1 with $\mu^-=1, \mu^+=1000$.

N	$ e_{1,h} _{0,\Omega}$	r	$ e_{2,h} _{0,\Omega}$	r	$ e_{3,h} _{0,\Omega}$	r	$ e_1 _{1,\Omega}$	r	$ e_{2} _{1,\Omega}$	r
8	7.26e-03	NA	7.25e-03	NA	1.15e-00	NA	7.19e-02	NA	7.12e-02	NA
16	2.04e-03	1.83	2.04e-03	1.83	7.56e-01	0.61	3.87e-02	0.89	3.82e-02	0.89
32	8.02e-04	1.34	8.02e-04	1.34	4.90e-01	0.63	2.09e-02	0.89	2.09e-02	0.87
64	1.19e-04	2.75	1.19e-04	2.75	2.19e-01	1.16	8.74e-03	1.26	8.74e-03	1.26
128	2.07e-05	2.53	2.07e-05	2.53	8.49e-02	1.37	4.32e-03	1.02	4.31e-03	1.02

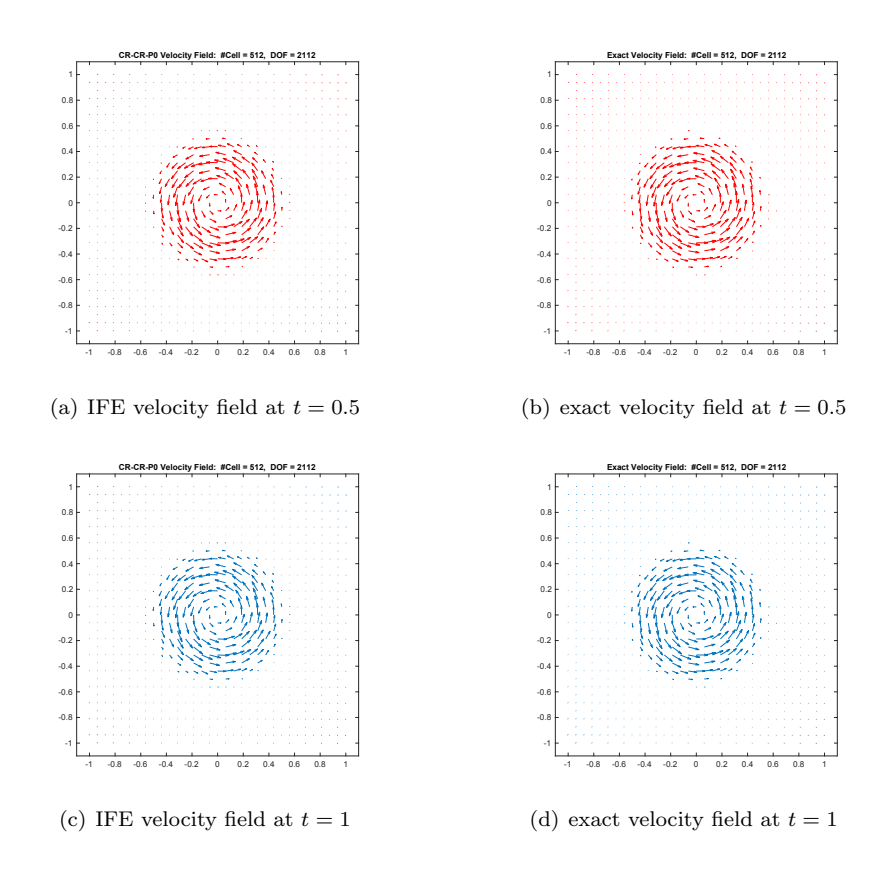


FIGURE 9. CR- P_0 IFE velocity field \boldsymbol{u}_h and exact velocity field \boldsymbol{u} at t=0.5 and t=1, when $\mu^-=1$, $\mu^+=1000$, N=16.

In Tables 7 and 8, we present the errors and the convergence rates of the CR- P_0 IFE solutions at t=1 when the contrast in viscosity coefficient is modest $(\mu^-,\mu^+)=(1,10)$ and relatively large $(\mu^-,\mu^+)=(1,1000)$, respectively. At each time step, it takes about three iterations for the Newton's method to converge, by selecting $\epsilon_0=10^{-8}$ in (31). Those tables demonstrate that the convergence rates are optimal. We plot the numerical solutions and exact solutions for the first component of the velocity at t=0.5 and t=1, when the contrast of the viscosity coefficients is $(\mu^-,\mu^+)=(1,10)$ in Figure 8 with the division of the domain N=128. According to those graphs, the numerical solutions at different time levels simulate the exact solution well and are resolved accurately around the interface. In addition, for the high-contrast viscosity coefficients where $(\mu^-,\mu^+)=(1,1000)$, we plot the numerical velocity field u_h and exact velocity field u in Figure 9 at t=0.5 and t=1, respectively, when the division of the domain is N=16. And the results

indicate that at these two different time levels, the numerical velocity field captures the features of exact velocity field well even on the mesh that is relatively coarse.

Example 5. (Unsteady NSE with a moving circular interface: variant radius) In this example, we consider a time-dependent NS interface problem described by (1) with a moving circular interface where the radius varies with respect to time : $\Gamma(x,y,t) = \{(x,y,t): x^2+y^2-(r(t))^2=0\}$, where $r(t) = (0.3(\frac{1}{2}\sin(2\pi t)+1))^{\frac{1}{2}}$, $t \in [0,1]$. The interface splits the domain Ω into two subdomains: $\Omega^-(t) = \{(x,y,t): x^2+y^2-(r(t))^2 < 0\}$ and $\Omega^+(t) = \{(x,y,t): x^2+y^2-(r(t))^2 > 0\}$. The function f in (1a) is generated with the following exact solution f and f:

(46)
$$\mathbf{u}(x,y,t) = \begin{cases} u_1(x,y,t) = \begin{cases} \frac{1}{\mu^-} y \Gamma(x,y,t), & \text{if } (x,y) \in \Omega^-(t), \\ \frac{1}{\mu^+} y \Gamma(x,y,t), & \text{if } (x,y) \in \Omega^+(t), \end{cases} \\ u_2(x,y,t) = \begin{cases} \frac{1}{\mu^-} x \Gamma(x,y,t), & \text{if } (x,y) \in \Omega^-(t), \\ -\frac{1}{\mu^+} x \Gamma(x,y,t), & \text{if } (x,y) \in \Omega^+(t), \end{cases}$$

(47)
$$p(x,y) = \frac{1}{10}(x^3 - y^3).$$

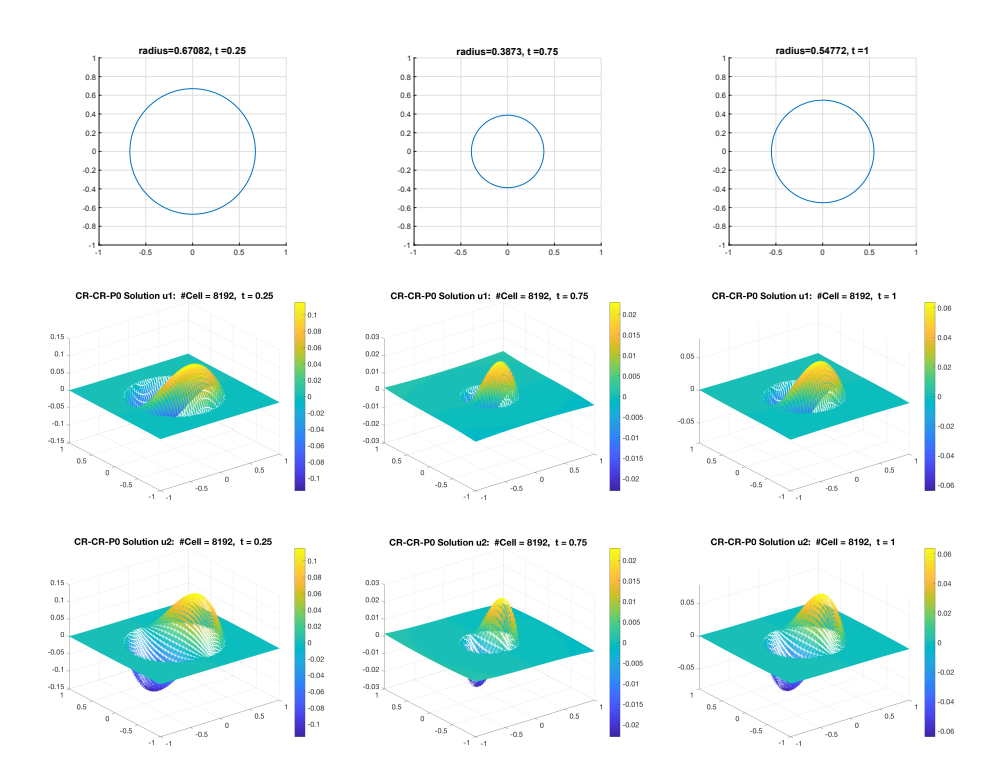


FIGURE 10. CR- P_0 IFE solutions in Example 5 with $\mu^-=1, \mu^+=1000$ at t=0.25, 0.75 and 1, on a 64×64 mesh . (Top plots: interface locations; middle: IFE solutions $u_{1,h}$; bottom: IFE solutions $u_{2,h}$.)

Selecting the division of the time interval M=N/2, Table 9 reports the errors of backward-Euler IFE solutions obtained by (34) at the final time level (t=1) for moderate contrast of viscosity coefficients $(\mu^-, \mu^+) = (1, 10)$; Table 10 reports the

TABLE 9. Errors of IFE solutions for Example 5 at t=1 with $(\mu^-, \mu^+) = (1, 10), M = N/2$.

N	$ e_{1,h} _{0,\Omega}$	r	$ e_{2,h} _{0,\Omega}$	r	$ e_{3,h} _{0,\Omega}$	r	$ e_1 _{1,\Omega}$	r	$ e_2 _{1,\Omega}$	r
8	6.44e-03	NA	6.43e-03	NA	8.54e-02	NA	1.36e-01	NA	1.41e-01	NA
16	1.88e-03	1.78	1.88e-03	1.78	4.60e-02	0.89	6.78e-02	1.01	6.68e-02	1.09
32	5.78e-04	1.70	5.78e-04	1.70	2.19e-02	1.07	3.37e-02	1.01	3.37e-02	0.99
64	2.15e-04	1.43	2.15e-04	1.43	9.65e-03	1.18	1.72e-02	0.97	1.72e-02	0.97
128	9.48e-05	1.18	9.48e-05	1.18	4.66e-03	1.05	8.68e-03	0.98	8.66e-03	0.99

TABLE 10. Errors of IFE solutions for Example 5 at t=1 with $(\mu^-, \mu^+) = (1, 1000), M = N/2$.

N	$ e_{1,h} _{0,\Omega}$	r	$ e_{2,h} _{0,\Omega}$	r	$ e_{3,h} _{0,\Omega}$	r	$ e_1 _{1,\Omega}$	r	$ e_2 _{1,\Omega}$	r
8	1.11e-02	NA	1.12e-02	NA	1.69e + 00	NA	1.36e-01	NA	1.36e-01	NA
16	2.78e-03	2.00	2.78e-03	2.00	8.80e-01	0.95	6.52e-02	0.96	6.52e-02	1.06
32	8.92e-04	1.64	8.92e-04	1.64	4.10e-01	1.10	3.38e-02	0.97	3.38e-02	0.95
64	1.31e-04	2.77	1.31e-04	2.77	1.64e-01	1.32	1.58e-02	1.09	1.58e-02	1.09
128	3.17e-05	2.05	3.17e-05	2.05	6.23e-02	1.40	7.98e-03	0.99	7.96e-03	0.99

TABLE 11. Errors of IFE solutions for Example 5 at t=1 with $(\mu^-, \mu^+) = (1, 10), M = N^2/8$.

N	$ e_{1,h} _{0,\Omega}$	r	$ e_{2,h} _{0,\Omega}$	r	$ e_{3,h} _{0,\Omega}$	r	$ e_1 _{1,\Omega}$	r	$ e_2 _{1,\Omega}$	r
8	6.39e-03	NA	6.39e-03	NA	8.17e-02	NA	1.34e-01	NA	1.39e-01	NA
1										
16	1.73e-03	1.89	1.73e-03	1.88	4.45e-02	0.88	6.68e-02	1.01	6.59e-02	1.08
32	4.52e-04	1.94	4.52e-04	1.94	2.13e-02	1.06	3.34e-02	1.00	3.34e-02	0.98
64	1.16e-04	1.96	1.16e-04	1.96	9.45e-03	1.17	1.71e-02	0.97	1.71e-02	0.97
128	2.95e-05	1.98	2.95e-05	1.98	4.58e-03	1.04	8.65e-03	0.98	8.64e-03	0.98

TABLE 12. Errors of IFE solutions for Example 5 at t=1 with $(\mu^-, \mu^+) = (1, 1000), M = N^2/8$.

N	$ e_{1,h} _{0,\Omega}$	r	$ e_{2,h} _{0,\Omega}$	r	$ e_{3,h} _{0,\Omega}$	г	$ e_1 _{1,\Omega}$	r	$ e_{2} _{1,\Omega}$	r
8	1.17e-02	NA	1.17e-02	NA	1.64e + 00	NA	1.30e-01	NA	1.36e-01	NA
16	3.36e-03	1.81	3.36e-03	1.81	8.48e-01	0.95	6.72e-02	0.95	6.60e-02	1.05
32	9.79e-04	1.78	9.79e-04	1.78	4.05e-01	1.07	3.42e-02	0.97	3.42e-02	0.95
64	1.63e-04	2.59	1.63e-04	2.59	1.63e-01	1.32	1.59e-02	1.11	1.59e-02	1.11
128	3.43e-05	2.25	3.43e-05	2.25	6.20e-02	1.39	7.98e-03	0.99	7.96e-03	1.00

errors for the situation of high contrast coefficients $(\mu^-, \mu^+) = (1, 1000)$. Tables 11 and 12 report the errors when selecting $M = N^2/8$. The numerical results are consistent with the theoretical optimal convergence rates: $\mathcal{O}(h^2 + \tau)$ for errors in L^2 norm and $\mathcal{O}(h+\tau)$ in H^1 semi-norm of the velocities; and $\mathcal{O}(h+\tau)$ for errors in L^2 norm of the pressure. Figure 10 shows the IFE solutions u_1 and u_2 at t=0.25, 0.75 and t=1 respectively, on a 64×64 mesh, when $(\mu^-, \mu^+)=(1, 1000)$.

Example 6. (Unsteady NSE with a moving circular interface: moving center) In this example, we consider a time-dependent NS interface problem described by (1) with a moving circular interface where its center is moving from the centroid of the domain to the upper right corner: $\Gamma(x,y,t) = \{(x,y,t): (x-0.2t)^2+(y-0.2t)^2-0.3=0\}, t\in [0,1].$ The interface splits the domain Ω into two subdomains: $\Omega^-(t)=\{(x,y,t): (x-0.2t)^2+(y-0.2t)^2-0.3>0\}$ and $\Omega^+(t)=\{(x,y,t): (x-0.2t)^2+(y-0.2t)^2-0.3>0\}$. The function f in (1a) is generated with the following exact solution f and f:

$$\mathbf{u}(x,y,t) = \begin{cases} u_1(x,y,t) = \begin{cases} \frac{1}{\mu^-}(y-0.2t)\Gamma(x,y,t), & \text{if } (x,y) \in \Omega^-(t), \\ \frac{1}{\mu^+}(y-0.2t)\Gamma(x,y,t), & \text{if } (x,y) \in \Omega^+(t), \\ -\frac{1}{\mu^-}(x-0.2t)\Gamma(x,y,t), & \text{if } (x,y) \in \Omega^-(t), \\ -\frac{1}{\mu^+}(x-0.2t)\Gamma(x,y,t), & \text{if } (x,y) \in \Omega^+(t), \end{cases}$$

Table 13. Errors of IFE solutions for Example 6 at t=1 with $(\mu^-, \mu^+) = (1, 10), M = N^2/8$.

N	$ e_{1,h} _{0,\Omega}$	r	$ e_{2,h} _{0,\Omega}$	r	$ e_{3,h} _{0,\Omega}$	г	$ e_1 _{1,\Omega}$	r	$ e_{2} _{1,\Omega}$	r
8	6.58e-03	NA	6.57e-03	NA	1.06e-01	NA	1.31e-01	NA	1.31e-01	NA
16	1.80e-03	1.87	1.80e-03	1.87	4.73e-02	1.17	6.96e-02	0.91	6.93e-02	0.92
32	4.63e-04	1.96	4.63e-04	1.96	2.21e-02	1.10	3.45e-02	1.01	3.43e-02	1.01
64	1.18e-04	1.97	1.18e-04	1.97	1.05e-02	1.08	1.74e-02	0.99	1.74e-02	0.98
128	2.99e-05	1.98	2.99e-05	1.98	5.04e-03	1.05	8.72e-03	1.00	8.71e-03	0.99

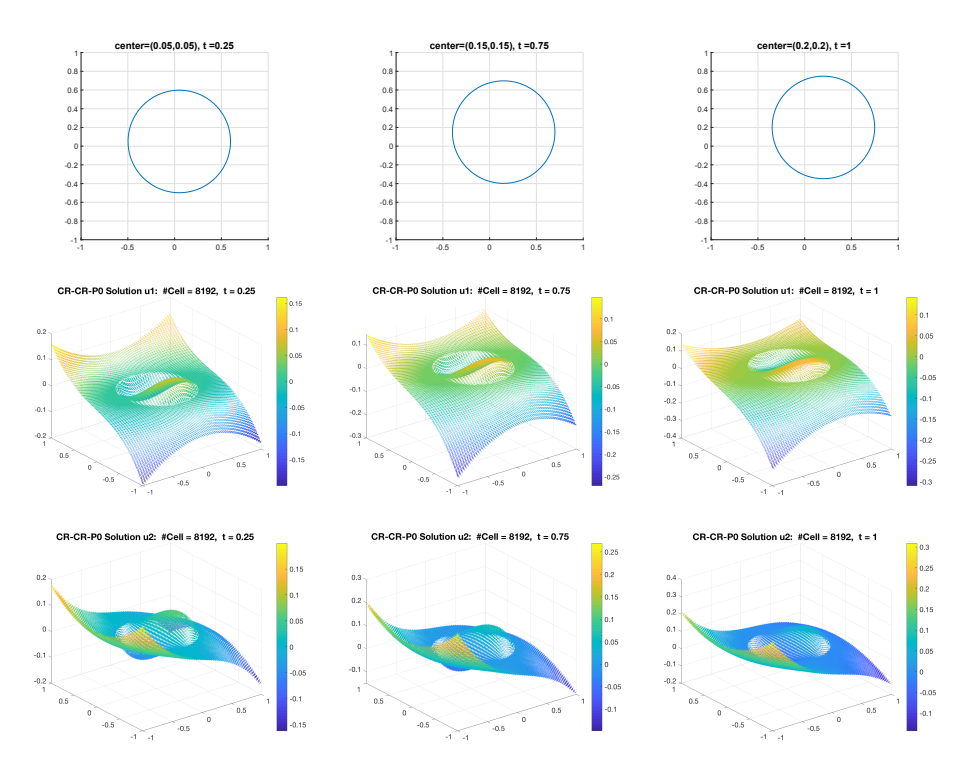


FIGURE 11. CR- P_0 IFE solutions in Example 6 with $\mu^-=1, \mu^+=10$ at t=0.25, 0.75 and 1, on a 64×64 mesh. (Top plots: interface locations; middle: IFE solutions $u_{1,h}$; bottom: IFE solutions $u_{2,h}$.)

TABLE 14. Errors of IFE solutions for Example 6 at t=1 with $(\mu^-, \mu^+) = (1, 1000), M = N^2/8$.

N	$ e_{1,h} _{0,\Omega}$	r	$ e_{2,h} _{0,\Omega}$	r	$ e_{3,h} _{0,\Omega}$	r	$ e_1 _{1,\Omega}$	r	$ e_2 _{1,\Omega}$	r
8	1.32e-02	NA	1.32e-02	NA	1.25e+00	NA	1.40e-01	NA	1.40e-01	NA
16	4.93e-03	1.42	4.93e-03	1.42	8.78e-01	0.51	7.98e-02	0.81	7.95e-02	0.82
32	9.48e-04	2.38	9.48e-04	2.38	4.18e-01	1.07	3.36e-02	1.25	3.34e-02	1.25
64	1.73e-04	2.45	1.73e-04	2.45	1.77e-01	1.24	1.60e-02	1.07	1.60e-02	1.06
128	3.43e-05	2.33	3.43e-05	2.33	6.53e-02	1.44	7.97e-03	1.01	7.95e-03	1.01

(49)
$$p(x,y) = \frac{1}{10}(x^3 - y^3).$$

Letting $M=N^2/8$, Table 13 and Table 14 report the errors of backward-Euler IFE solutions at the final time level (t=1) for moderate contrast $(\mu^-,\mu^+)=(1,10)$ and high contrast $(\mu^-,\mu^+)=(1,1000)$ of viscosity coefficients. The optimal orders of convergence are observed. Figure 11 shows the IFE solutions u_1 and u_2 at t=0.25,0.75 and t=1 respectively, on a 64×64 mesh, when $(\mu^-,\mu^+)=(1,10)$.

5. Conclusion

In this paper, we developed a nonconforming immersed finite element method for Navier-Stokes equations with fixed and moving interfaces based on $\operatorname{CR-}P_0$ IFE spaces. A semi-discrete scheme and backward Euler scheme implemented with Newton's method are designed for the interface problems. Numerical examples are provided to demonstrate the accuracy of the proposed IFE methods with different configurations of interfaces and discontinuous viscosity coefficients. The optimal orders of convergence of the IFE solutions are observed. The IFE solutions on interface-unfitted meshes are compared with classical CR finite element solutions on body-fitting meshes, and the accuracies of both methods are similar. Therefore the proposed IFE methods can solve Navier-Stokes interface problems accurately on interface-independent meshes.

Acknowledgements

Jin Wang is partially supported by National Science Foundation Grants DMS-1951345 and DMS-1913180. Xu Zhang is partially supported by National Science Foundation Grant DMS-2110833, the ORAU Ralph E. Powe Junior Faculty Enhancement Award, and the Oklahoma State University Arts and Sciences Research Grant.

References

- Slimane Adjerid, Nabil Chaabane, and Tao Lin. An immersed discontinuous finite element method for stokes interface problems. Comput. Methods Appl. Mech. Engrg., 293:170–190, 2015
- [2] Slimane Adjerid, Ruchi Guo, and Tao Lin. High degree immersed finite element spaces by a least squares method. Int. J. Numer. Anal. Model., 14(4-5):604-626, 2017.
- [3] Slimane Adjerid, Tao Lin, and Qiao Zhuang. Error estimates for an immersed finite element method for second order hyperbolic equations in inhomogeneous media. J. Sci. Comput., 84(35):https://doi.org/10.1007/s10915-020-01283-0, 2020.
- [4] Maximilian Balmus, Andr Massing, Johan Hoffman, Reza Razavi, and David A. Nordsletten. A partition of unity approach to fluid mechanics and fluidstructure interaction. Computer Methods in Applied Mechanics and Engineering, 362:112842, 2020.
- [5] E. Burman and P. Hansbo. Fictitious domain finite element methods using cut elements:
 I. a stabilized Lagrange multiplier method. Comput. Methods. Appl. Mech., 199:2680–2686, 2010.
- [6] E. Burman and P. Hansbo. Fictitious domain finite element methods using cut elements: II. a stabilized Nitsche method. Appl. Num. Math., 62:328–341, 2012.
- [7] Erik Burman, Susanne Claus, Peter Hansbo, Mats G. Larson, and André Massing. Cutfem: Discretizing geometry and partial differential equations. International Journal for Numerical Methods in Engineering, 104(7):472–501, 2015.
- [8] Yuan Chen and Xu Zhang. A P₂ P₁ partially penalized immersed finite element method for stokes interface problems. Int. J. Numer. Anal. Model., 18(1):120-141, 2015.
- [9] A. Christafakis, J. Alexopoulos, and S. Tsangaris. Modelling of two-phase incompressible flows in ducts. Applied Mathematical Modeling., 33:1201–1212, 2009.
- [10] Konstantinos Chrysafinos and Noel J. Walkington. Discontinuous Galerkin approximations of the stokes and Navier-stokes equations. Math. Comp., 79(272):2135–2167, 2010.
- [11] Susanne Claus and Pierre Kerfriden. A cutfem method for two-phase flow problems. Comput. Methods Appl. Mech. Engrg., 348:185–206, 2019.
- [12] N. G. Cogan and Robert D. Guy. Multiphase flow models of biogels from crawling cells to bacterial biofilms. HFSP J., 4(1):11–25, 2010.
- [13] Wei-Feng Dai, Peng Wu, and Guang-Miao Liu. A two-phase flow approach for modeling blood stasis and estimating the thrombosis potential of a ventricular assist device. Int. J. Artif. Organs., page doi: 10.1177/0391398820975405, 2020.
- [14] John Dolbow, Nicolas Moës, and Ted Belytschko. An extended finite element method for modeling crack growth with frictional contact. Comput. Methods Appl. Mech. Engrg., 190(51-52):6825–6846, 2001.

- [15] E. Ferrer and R.H.J. Willden. A high order discontinuous Galerkin finite element solver for the incompressible Navier-Stokes equations. Computers & Fluids, 46:224–230, 2010.
- [16] Michel Fortin. Finite element solution of the Navier-Stokes equations. Acta Numerica, 2:239 – 284, 1993.
- [17] Thomas Frachon and Sara Zahedi. A cut finite element method for incompressible two-phase Navier-Stokes flows. Journal of Computational Physics, 384:77–98, 2019.
- [18] Vivette Girault and Pierre-Arnaud Raviart. Finite Element Methods for Navier-Stokes Equations. Springer, Berlin, Heidelberg, 1987.
- [19] R. Guo and T. Lin. A higher degree immersed finite element method based on a Cauchy extension. SIAM J. Numer. Anal., 57(4):1545–1573, 2019.
- [20] Ruchi Guo. Solving parabolic moving interface problems with dynamical immersed spaces on unfitted meshes: Fully discrete analysis. SIAM J. Numer. Anal., 59(2):797–828, 2021.
- [21] Ruchi Guo and Tao Lin. A group of immersed finite element spaces for elliptic interface problems. IMA J.Numer. Anal., 39:482–511, 2017.
- [22] Ruchi Guo, Tao Lin, and Yanping Lin. Approximation capabilities of immersed finite element spaces for elasticity interface problems. Numerical Methods for Partial Differential Equations, 35(3):1243–1268, 2019.
- [23] Ruchi Guo, Tao Lin, and Yanping Lin. Error estimates for a partially penalized immersed finite element method for elasticity interface problems. ESAIM Math. Model. Numer. Anal., 54(1):1–24, 2020.
- [24] Xiaoming He, Tao Lin, and Yanping Lin. Immersed finite element methods for elliptic interface problems with non-homogeneous jump conditions. Int. J. Numer. Anal. Model., 8(2):284–301, 2011.
- [25] Xiaoming He, Tao Lin, Yanping Lin, and Xu Zhang. Immersed finite element methods for parabolic equations with moving interface. Numer. Methods Partial Differential Equations, 29(2):619-646, 2013.
- [26] F. Heimann, C. Engwer, O. Ippisch, and P. Bastian. An unfitted interior penalty discontinuous Galerkin method for incompressible Navier-Stokes two-phase flow. Int. J. Numer. Meth. Fluids., 71:269–293, 2013.
- [27] Xiaozhe Hu, Lin Mu, and Xiu Ye. A weak Galerkin finite element method for the Navier-Stokes equations. J. Comput. Appl. Math., 362:614–625, 2017.
- [28] Volker John. Finite element methods for incompressible flow problems, volume 51 of Springer Series in Computational Mathematics. Springer, Cham, 2016.
- [29] Derrick Jones and Xu Zhang. A class of nonconforming immersed finite element methods for stokes interface problems. J. Comput. Appl. Math., 392:113493, 2021.
- [30] Derrick Jones and Xu Zhang. A conforming-nonconforming mixed immersed finite element method for unsteady stokes equations with moving interfaces. Electronic Research Archive, doi: 10.3934/era.2021032, 2021.
- [31] Derrick T. Jones. A Class of Immersed Finite Element Methods for Stokes Interface Problems. ProQuest LLC, Ann Arbor, MI, 2021. Thesis (Ph.D.)—Mississippi State University.
- [32] Z. Li, T. Lin, Y. Lin, and R. C. Rogers. An immersed finite element space and its approximation capability. Numer. Methods Partial Differential Equations, 20(3):338–367, 2004.
- [33] Zhilin Li and Kazufumi Ito. The immersed interface method, volume 33 of Frontiers in Applied Mathematics. Society for Industrial and Applied Mathematics (SIAM), Philadelphia, PA, 2006. Numerical solutions of PDEs involving interfaces and irregular domains.
- [34] Zhilin Li and Ming-Chih Lai. The immersed interface method for the Navier-Stokes equations with singular forces. J. Comput. Phys., 171(2):822-842, 2001.
- [35] Tao Lin, Yanping Lin, and Xu Zhang. A method of lines based on immersed finite elements for parabolic moving interface problems. Adv. Appl. Math. Mech., 5(4):548–568, 2013.
- [36] Tao Lin, Yanping Lin, and Xu Zhang. Partially penalized immersed finite element methods for elliptic interface problems. SIAM J. Numer. Anal., 53(2):1121–1144, 2015.
- [37] Tao Lin, Dongwoo Sheen, and Xu Zhang. Nonconforming immersed finite element methods for elliptic interface problems. J. Sci. Comput., 79:442–463, 2019.
- [38] Tao Lin, Qing Yang, and Xu Zhang. Partially penalized immersed finite element methods for parabolic interface problems. Numer. Meth. Partial Diff. Eqn., 31(6):1925–1947, 2015.
- [39] Tao Lin and Xu Zhang. Linear and bilinear immersed finite elements for planar elasticity interface problems. J. Comput. Appl. Math., 236(18):4681–4699, 2012.
- [40] Tao Lin and Qiao Zhuang. Optimal error bounds for partially penalized immersed finite element methods for parabolic interface problems. J. Comput. Appl. Math., 366:112401, 2020.

- [41] Jinhui Liu, Yang Ju, and Yingqing Zhang Wenbo Gong. Preferential paths of air-water twophase flow in porous structures with special consideration of channel thickness effects. Scientific Reports, 4:16204, 2019.
- [42] Chuwen Ma, Qinghai Zhang, and Weiying Zheng. A high-order fictitious-domain method for the advection-diffusion equation on time-varying domain. arXiv:2104.01870, 2021.
- [43] Chuwen Ma and Weiying Zheng. High-order finite element methods for nonlinear convectiondiffusion equation on time-varying domain. arXiv:2106.16026, 2021.
- [44] J.M. Melenk and I. Babuka. The partition of unity finite element method: Basic theory and applications. Computer Methods in Applied Mechanics and Engineering, 139(1):289–314, 1996.
- [45] A. Montlaur, Fernandez-Mendez, J. Peraire, and A. Huerta. Discontinuous Galerkin methods for the Navier-Stokes equations using solenoidal approximations. Int. J. Numer. Meth. Fluids, 64:549–564, 2009.
- [46] Lin Mu. A pressure-robust weak Galerkin finite element method for Navier-Stokes equations. arxiv.org/abs/2011.11526, pages 1–30, 2020.
- [47] Beatrice Riviere and Shirin Sardar. Penalty-free discontinuous Galerkin methods for incompressible Navier-Stokes equations using solenoidal approximations. Math. Model. Meth. Appl. Sci, 24(6):1217–1236, 2014.
- [48] B. Schott and W.A. Wall. A new face-oriented stabilized xfem approach for 2d and 3d incompressible navierstokes equations. Computer Methods in Applied Mechanics and Engineering, 276:233–265, 2014.
- [49] Jin Wang and Gregory Baker. A numerical algorithm for viscous incompressible interfacial flows. J. Comput. Phys., 228:5470–5489, 2009.
- [50] Qing Yang and Xu Zhang. Discontinuous galerkin immersed finite element methods for parabolic interface problems. J. Comput. Appl. Math., 299:127–139, 2016.
- [51] Jiachuan Zhang, Kai Zhang, Jingzhi Li, and Xiaoshen Wang. A weak Galerkin finite element method for the navier-stokes equations. Commun. Comput. Phys., 23:706–746, 2018.
- [52] Y.C. Zhou, Jiangguo Liu, and Dennis L. Harry. A matched interface and boundary method for solving multi-flow navierstokes equations with applications to geodynamics. Journal of Computational Physics, 231(1):223–242, 2012.
- [53] Y.C. Zhou and G.W. Wei. On the fictitious-domain and interpolation formulations of the matched interface and boundary (MIB) method. Journal of Computational Physics, 219(1):228–246, 2006.
- [54] Qiao Zhuang and Ruchi Guo. High degree discontinuous petrov-galerkin immersed finite element methods using fictitious elements for elliptic interface problems. J. Comput. Appl. Math., pages 560–573, 2019.

Department of Mathematics, University of Tennessee at Chattanooga, Chattanooga, TN 37403, $_{\rm LIGA}$

 $E ext{-}mail: jin-wang02@utc.edu}$

Department of Mathematics, Oklahoma State University, Stillwater, OK 74078, USA E-mail: xzhang@okstate.edu

Department of Mathematical Sciences, Worcester Polytechnic Institute, Worcester, MA 01609, USA

 $E ext{-}mail: qzhuang@wpi.edu$